White Rose Research Online
eprints@whiterose.ac.uk
https://eprints.whiterose.ac.uk
Universities of Leeds, Sheffield and York

Deposited via The University of Sheffield.

White Rose Research Online URL for this paper:
https://eprints.whiterose.ac.uk/id/eprint/110519/

Version: Accepted Version

Article:

Bhattacharya, P. and Siegmund, T. (2014) Computational modeling of vibration-induced systemic hydration of vocal folds over a range of phonation conditions. International Journal for Numerical Methods in Biomedical Engineering, 30 (10). pp. 1019-1043. ISSN: 2040-7939

https://doi.org/10.1002/cnm2642

Reuse

Items deposited in White Rose Research Online are protected by copyright, with all rights reserved unless indicated otherwise. They may be downloaded and/or printed for private study, or other acts as permitted by national copyright laws. The publisher or other rights holders may allow further reproduction and re-use of the full text version. This is indicated by the licence information on the White Rose Research Online record for the item.

Takedown

If you consider content in White Rose Research Online to be in breach of UK law, please notify us by emailing eprints@whiterose.ac.uk including the URL of the record and the reason for the withdrawal request.

UNIVERSITY OF LEEDS
University of Sheffield
UNIVERSITY of York

INTERNATIONAL JOURNAL FOR NUMERICAL METHODS IN BIOMEDICAL ENGINEERING
Int. J. Numer. Meth. Biomed. Engng. 2013; **00**:1–**??**
Published online in Wiley InterScience (www.interscience.wiley.com). DOI: 10.1002/cnm

Computational modeling of vibration-induced systemic hydration of vocal folds over a range of phonation conditions

Pinaki Bhattacharya[1]* and Thomas Siegmund[1]

[1] *School of Mechanical Engineering, Purdue University, West Lafayette, USA.*

SUMMARY

Predicting phonation conditions that are benign to voice health remains a biomechanically relevant problem. Our objective is to provide insight into vocal fold (VF) hydration based on continuum-based VF models which are able to compute VF stresses during phonation and a scheme for the extraction and generalization of such computational data based on the principle of linear superposition. Since VF tissue is poroelastic, spatial gradients of VF hydrostatic stresses computed for a given phonation condition determine VF interstitial fluid flow. The present approach transforms, based on linear superposition principles, the computed interstitial fluid velocities at the particular phonation to those at an arbitrary phonation condition. Intersititial fluid flow characteristics for a range of phonation conditions are compared. For phonation conditions with no or moderate collision no dehydration per vibration cycle is predicted throughout the VF. For more severe collision conditions, tissue dehydration is restricted to a region close to the glottal surface. Interstitial fluid displacement in the VF is found to be heterogeneous and strongly dependent on the phonation condition. A phonation condition is found to exist for which dehydration peaks. The proposed method significantly expands the scope and relevance of conducting isolated numerical simulations of VF vibration. Copyright © 2013 John Wiley & Sons, Ltd.

Received . . .

KEY WORDS: vocal folds; systemic hydration; interstitial fluid; computational modeling; stresses; vibration; collision

1. INTRODUCTION

High-fidelity computational models are becoming available in the literature [1, 2, 3, 4, 5, 6, 7, 8, 9, 10] that are capable of simulating flow–structure interaction (FSI) between glottal airflow and three-dimensional vocal folds (VFs). In these models it is possible to determine stresses inside the VF tissue as it vibrates during FSI. Such a determination of VF stresses is not possible from experimental studies alone. A biomechanically relevant interpretation of stresses can be made by relating the stresses to the movement of interstitial fluid within the VF, also known as VF systemic

---

*Correspondence to: School of Mechanical Engineering, Purdue University, West Lafayette, USA. E-mail: pbhattac@purdue.edu

Contract/grant sponsor: NIDCD; contract/grant number: 5R01DC008290-05

Copyright © 2013 John Wiley & Sons, Ltd.

hydration [11]. For instance, in a recent article the interstitial fluid in the VF tissue was considered to be driven by the gradients of hydrostatic stresses [2], a notion based on the knowledge that VF tissue is biphasic i.e. it comprises a porous elastic solid phase which is fully saturated by a fluid phase ('interstitial' fluid). It has been shown that a biphasic material with a porous elastic solid skeleton can exhibit a time-dependent response. Time-dependent responses such as creep and stress relaxation are equivalent to macroscale viscoelastic behavior [12, 13]. Biphasic material analysis has been carried out for VF tissue [14, 15, 16, 17, 18, 19] as well as for other biological tissues (e.g. bone [20]). Computations performed in [2] indicated that VF vibration-induced systemic hydration could be significant. Therefore, analysis of systemic hydration is a potentially clinically relevant end-point of computational modeling of VF FSI.

The purpose of this paper is to present a methodology to create insight into the hydration conditions in vibrating and colliding vocal folds. Coupled flow structure interaction computations can in principle provide such information, are limited in that such computations have to be performed case by case. The approach described in the paper demonstrates how to extract pertinent information from flow structure computations and how to use this information, i.e. to construct a map delineating hydration conditions relative to vibration and collision of the vocal fold system.

A pertinent extension of this analysis is to determine vibration-induced systemic hydration in a subject-specific VF over a range of phonation conditions. However, a typical FSI computation involves significant computational overhead, even when performed for a subject-specific VF (fixed geometry and tissue properties) and a single phonation/airflow condition. Thus insights regarding systemic hydration appear to be restricted to the specific phonation condition under which the computation was performed. This paper investigates the possibility of extending such insights obtained from a single computation to a range of phonation conditions.

The approach used in this study (detailed in section 2) comprises three steps, namely, decomposition, scaling and superposition. In the decomposition step VF displacement and hydrostatic stress are decomposed into average, fluctuation and collision-induced contributions. These contributions correspond respectively to the well-described notions of 'dc-offset', 'ac-part' and 'baseline truncation' in voice literature [21, 22]. The decomposition strategy is motivated by the current understanding of phonation conditions. In the absence of phonation-induced self-sustained vibrations only the 'dc-offset' is present. In contrast, for phonation conditions characterized by low-amplitude vibrations (e.g. falsetto register [23]) only a small amount of 'baseline truncation' is found. Finally, the most common phonation conditions (e.g. in modal voice [23]) exhibit a significant degree of all three contributions.

The scaling step follows the continuuum mechanical description of the VF domain. Continuum mechanics implies that VF stress depends on VF geometry, VF tissue properties and phonation condition dependent fluid (airflow) loading applied at the VF boundary. Hence the dependence on phonation conditions is removed by scaling with respect to factors representing glottal airflow loading. The scaling factors are derived from average transglottal pressure difference (TPD) [21] and superior-surface displacement. This approach is supported by state-of-the-art capabilities in *in vivo* measurement of TPD [24, 25, 26] and of superior-surface motion ([27, 28, 29] among others). The scaling step is applied separately to the average, fluctuation and collision-induced contributions to the hydrostatic stress and to the interstitial fluid velocity (based on the spatial gradient of hydrostatic stress), in that order.

Copyright © 2013 John Wiley & Sons, Ltd.

Prepared using cnmauth.cls
DOI: 10.1002/cnm

In the final superposition step the total interstitial fluid velocity for an arbitrary (new) phonation condition is determined as the weighted sum of the scaled interstitial fluid velocity fields. The weights in the sum are the same scaling factors as in the previous step but their values correspond to the new phonation condition.

An underlying assumption in the method outlined above is that the strains in the VFs during phonation-induced vibration are small enough such that terms that are non-linear in strain can be neglected. Strains in VFs during self-sustained oscillations have been recorded experimentally in recent works [30, 31, 32, 33]. These studies show that during self-sustained oscillations and for a wide range of voiced speech strains on the superior surface of the VF tissue are small ($< 15\%$). Past work on characterizing the VF tissue has found that in this small strain regime the VF tissue response is predominantly linear [34, 35, 36]. Including this assumption not only simplifies the analysis, but also allows ready comparison of present results with a large body of literature on computational studies of VF dynamics where also the small-strain assumption was employed [37, 38, 39, 4, 40, 6]. In addition to the small vibration-induced strains there possibly exist large strains in the VFs due to pre-phonatory posturing. However, the effect of these large strains are already accounted for in a VF computational model e.g. by specifying a minimum pre-phonatory glottal width and a tangent modulus of elasticity of the VF tissue. Consequently, the small-strain assumption is valid under the limitation that the pre-phonatory conditions are held fixed.

In section 3 the computational model presented in [2] is reviewed. For the rest of the manuscript, this model serves as a working example of an FSI computation to which the above three-step method is applied. Yet, the method remains applicable to any FSI computation of VF self-sustained vibration including collision, as long as the VFs are deformable and the phonation-induced strains are small. Hence a wide variety of tissue constitutive behaviors and pre-phonatory geometries can be analyzed by minor adaptations.

As mentioned earlier the main goal of this study is to compare systemic hydration across a range of phonation conditions. Towards this goal in sections 4.1 and 4.2 results are presented from the application of decomposition and scaling for the example FSI computation above [2]. Thus spatial and temporal characteristics of the scaled contributions to interstitial fluid velocity are quantified in the VF interior. In section 4.3 interstitial fluid velocities are computed over a range of phonation conditions using the superposition method. For interstitial fluid particles starting at different locations on the mid-coronal plane, interstitial fluid trajectories over vibration cycles are analyzed as a function of phonation condition parameters. A novel hydration map analysis is introduced by which the per-cycle displacement of interstitial fluid is quantified as a function of phonation condition parameters. Demonstration of the derivation of the continuum mechanics-based hydration map for an example VF achieves the main goal of this study.

The biomechanical relevance of the hydration map is discussed in section 5 by shifting focus to a schematic of the hydration map that highlights its salient features qualitatively. Evidence in literature suggests that the phonation condition parameters, namely TPD and superior-surface displacement component are not independent of each other [22]. The implication of this condition on the interpretation of a typical hydration map is presented. Landmark phonation conditions corresponding to maximum collision without dehydration and maximum dehydration are depicted on the hydration map.

2. METHOD

2.1. Decomposition of Superior-Surface Displacement and Hydrostatic Stress

In the following, any location on the undeformed VF configuration is referred to by the position vector $\vec{X}$ which has components X_{is}, X_{ml} and X_{ap} in the mutually-perpendicular inferior–superior, medial–lateral and anterior–posterior directions respectively. Consider the medial–lateral component of displacement u_{ml} as a function of $\vec{X}$ and time t. In the following, $u_{\mathrm{ml}}(\vec{X},t)$ is considered to be negative when the particular VF corresponding to $\vec{X}$ is moving away from the opposing VF and considered to be positive when approaching it. A maximum open instant is defined as an instant when u_{ml} at pre-specified VF superior-surface location $\vec{X}_{\mathrm{SS}}$ attains its most negative value. Successive maximum open instants t_n and t_{n+1} identify the n-th VF vibration cycle (figure 1).

For a collision-free vibration cycle, the average quantity is determined

$$\bar{u}_{\mathrm{ml}}(\vec{X}_{\mathrm{SS}}) \equiv \frac{1}{t_p}\int_{t_n}^{t_{n+1}} u_{\mathrm{ml}}(\vec{X}_{\mathrm{SS}},t)\,\mathrm{d}t, \tag{1}$$

where $t_p \equiv t_{n+1} - t_n$ is the cycle time period. Within a cycle, consider the first instant $\bar{t}$ such that the condition $u_{\mathrm{ml}}(\vec{X}_{\mathrm{SS}},\bar{t}) = \bar{u}_{\mathrm{ml}}(\vec{X}_{\mathrm{SS}})$ is met. For VF locations $\vec{X} \neq \vec{X}_{\mathrm{SS}}$, the average displacement is approximated as

$$\bar{u}_{\mathrm{ml}}(\vec{X}) \equiv u_{\mathrm{ml}}(\vec{X},\bar{t}). \tag{2}$$

Over the vibration cycle, at all locations, the displacement fluctuates about the average,

$$\Delta u_{\mathrm{ml}}(\vec{X},t) = u_{\mathrm{ml}}(\vec{X},t) - \bar{u}_{\mathrm{ml}}(\vec{X}), \tag{3}$$

and is approximated as a product of an 'amplitude' $\Delta u_{\mathrm{ml},0}(\vec{X})$ and a time-variation $f(t)$, where

$$\Delta u_{\mathrm{ml},0}(\vec{X}) \equiv u_{\mathrm{ml}}(\vec{X},t_n) - \bar{u}_{\mathrm{ml}}(\vec{X}) \quad \text{and} \quad f(t) \equiv \frac{\Delta u_{\mathrm{ml}}(\vec{X}_{\mathrm{SS}},t)}{\Delta u_{\mathrm{ml},0}(\vec{X}_{\mathrm{SS}})}. \tag{4}$$

Note that $f(t)$ is based only on $\vec{X}_{\mathrm{SS}}$, and the approximation reduces to an identity at $\vec{X}_{\mathrm{SS}}$.

When the n-th vibration cycle involves VF collision (figure 2), the collision effects at $\vec{X}_{\mathrm{SS}}$ exist only inside a collision-interval $[t_{c,n}, t_{o,n}] \subset [t_n, t_{n+1}]$ (subscripts: c, closing and o, opening). Instants $t_{c,n}$ and $t_{o,n}$ must initially be estimated. Consider the motion of $\vec{X}_{\mathrm{C}}$, which is a medial-surface location in the same coronal plane as $\vec{X}_{\mathrm{SS}}$ and is undergoing substantial collision. Typically, the motion of $\vec{X}_{\mathrm{C}}$ is determined accurately in a computation and it can be used to estimate $t_{c,n}$ and $t_{o,n}$. Next, by using an interpolation method, the time-dependence of $u_{\mathrm{ml}}(\vec{X}_{\mathrm{SS}},t)$ outside the collision-interval is used to determine a 'virtual' collision-free displacement throughout the cycle and is referred to as $u_{\mathrm{ml},v}(\vec{X}_{\mathrm{SS}},t)$ (details in appendix A). For the vibration cycle with collision, the average and the fluctuation at $\vec{X}_{\mathrm{SS}}$ are defined as

$$\bar{u}_{\mathrm{ml}}(\vec{X}_{\mathrm{SS}}) \equiv \frac{1}{t_p}\int_{t_n}^{t_{n+1}} u_{\mathrm{ml},v}(\vec{X}_{\mathrm{SS}},t)\,\mathrm{d}t, \tag{5}$$

$$\Delta u_{\mathrm{ml}}(\vec{X}_{\mathrm{SS}},t) \equiv u_{\mathrm{ml},v}(\vec{X}_{\mathrm{SS}},t) - \bar{u}_{\mathrm{ml}}(\vec{X}_{\mathrm{SS}}), \tag{6}$$

Copyright © 2013 John Wiley & Sons, Ltd.
Prepared using cnmauth.cls

respectively. These expressions are similar to the corresponding ones in the collision-free cycle case, except that u_{ml} is now substituted with $u_{\mathrm{ml},v}$ on the right. Similar to before, $\bar{t}$ is defined from the condition $u_{\mathrm{ml},v}(\vec{X}_{\mathrm{SS}},\bar{t}) = \bar{u}_{\mathrm{ml}}(\vec{X}_{\mathrm{SS}})$ and the definition for $\Delta u_{\mathrm{ml},0}(\vec{X}_{\mathrm{SS}})$ is identical to that in (4). However, $f(t)$ is defined as

$$f(t) \equiv \frac{\Delta u_{\mathrm{ml},v}(\vec{X}_{\mathrm{SS}},t)}{\Delta u_{\mathrm{ml},0}(\vec{X}_{\mathrm{SS}})}, \tag{7}$$

although it is still based on $\vec{X}_{\mathrm{SS}}$ only. For locations other than $\vec{X}_{\mathrm{SS}}$, $\bar{u}_{\mathrm{ml}}(\vec{X})$ and $\Delta u_{\mathrm{ml},0}(\vec{X})$ are obtained from (2) and (4) respectively. The 'virtual' collision-free displacement at location $\vec{X} \neq \vec{X}_{\mathrm{SS}}$ is defined

$$u_{\mathrm{ml},v}(\vec{X},t) \equiv \bar{u}_{\mathrm{ml}}(\vec{X}) + \Delta u_{\mathrm{ml},0}(\vec{X}) f(t). \tag{8}$$

For all locations the collision-induced contribution to displacement is defined as

$$u_{\mathrm{ml},C}(\vec{X},t) \equiv u_{\mathrm{ml}}(\vec{X},t) - u_{\mathrm{ml},v}(\vec{X},t), \tag{9}$$

or,

$$u_{\mathrm{ml},C}(\vec{X},t) = u_{\mathrm{ml}}(\vec{X},t) - \left[\bar{u}_{\mathrm{ml}}(\vec{X}) + \Delta u_{\mathrm{ml},0}(\vec{X}) f(t)\right]. \tag{10}$$

The 'corrected' collision-interval $[t_{c,n}, t_{o,n}]$ is then set equal to the largest continuous interval in which $u_{\mathrm{ml},C}(\vec{X}_{\mathrm{SS}},t)$ is negative (up to a specified tolerance). Henceforth all collision induced contributions are set to zero outside this interval. A virtual overclosure is defined

$$u_{\mathrm{ml},C0}(\vec{X}_{\mathrm{SS}}) \equiv -\min\left[u_{\mathrm{ml},C}(\vec{X}_{\mathrm{SS}},t)\right] \quad \text{where } t \in [t_{c,n}, t_{o,n}], \tag{11}$$

and the condition $u_{\mathrm{ml},C0}(\vec{X}_{\mathrm{SS}}) = -u_{\mathrm{ml},C}(\vec{X}_{\mathrm{SS}}, t_{\max,n})$ is used to define the instant $t_{\max,n} \in [t_{c,n}, t_{o,n}]$. A non-dimensional time $\tilde{t}$ within the collision interval and a function $g(\tilde{t})$ dependent on it are defined as

$$\tilde{t} \equiv \frac{t - t_{o,n}}{t_{o,n} - t_{c,n}} \quad \text{and} \quad g(\tilde{t}) \equiv -\frac{u_{\mathrm{ml},C}(\vec{X}_{\mathrm{SS}},t)}{u_{\mathrm{ml},C0}(\vec{X}_{\mathrm{SS}})}, \tag{12}$$

These are used later to model the time-variation of collision-induced contributions.

The hydrostatic stress invariant is defined as

$$\sigma_H \equiv \frac{1}{3}\mathrm{tr}(\boldsymbol{\sigma}), \tag{13}$$

where tr is the trace operator and $\boldsymbol{\sigma}$ is the Cauchy stress tensor. Following the decomposition of the displacement $u_{\mathrm{ml}}(\vec{X}_{\mathrm{SS}},t)$, the quantities t_n, t_{n+1}, $\bar{t}$ and $f(t)$ are known. For a collision cycle, additionally, $t_{c,n}$, $t_{o,n}$ and $t_{\max,n}$ are known. The average, fluctuation amplitude, fluctuation, collision-induced contribution, and collision-induced amplitude of hydrostatic stress are defined as,

Copyright © 2013 John Wiley & Sons, Ltd.

Prepared using cnmauth.cls

respectively

$$\begin{aligned}
\bar{\sigma}_H(\vec{X}) &\equiv \sigma_H(\vec{X},\bar{t}), && (14)\\
\Delta\sigma_{H,0}(\vec{X}) &\equiv \sigma_H(\vec{X},t_n) - \bar{\sigma}_H(\vec{X}), && (15)\\
\Delta\sigma_H(\vec{X},t) &\equiv \Delta\sigma_{H,0}(\vec{X}) f(t), && (16)\\
\sigma_{H,C}(\vec{X},t) &\equiv \sigma_H(\vec{X},t) - \left[\bar{\sigma}_H(\vec{X}) + \Delta\sigma_H(\vec{X},t)\right], && (17)\\
\text{and} \quad \sigma_{H,C0}(\vec{X}) &\equiv \sigma_{H,C}(\vec{X},t_{\max,n}). && (18)
\end{aligned}$$

In case of a collision-free vibration cycle $\sigma_{H,C}(\vec{X},t)$ and $\sigma_{H,C0}(\vec{X})$ are defined to be identically zero.

2.2. *Scaling Hydrostatic Stress and Interstitial Fluid Velocity Contributions*

Following the continuum definition of VF tissue the hydrostatic stress at any VF location and the separate contributions to hydrostatic stress depend on: the external fluid loading and the geometry and constitutive properties of the VF domain. Of these external fluid loading is the only factor that depends on the phonation condition. Hence phonation condition related effects can be removed by scaling the above contributions as follows

$$\bar{\hat{\sigma}}_H(\vec{X}) \equiv \frac{\bar{\sigma}_H(\vec{X})}{\bar{p}}, \quad \Delta\hat{\sigma}_H(\vec{X},t) \equiv \frac{\Delta\sigma_H(\vec{X},t)}{\Delta u_{\mathrm{ml},0}(\vec{X}_{\mathrm{SS}})},$$
$$\text{and} \quad \hat{\sigma}_{H,C}(\vec{X},t) \equiv \frac{\sigma_{H,C}(\vec{X},t)}{\sqrt{u_{\mathrm{ml},C0}(\vec{X}_{\mathrm{SS}})}}, \tag{19}$$

where $\hat{\sigma}_H$ denotes scaled hydrostatic stress and $\bar{p}$ is the TPD averaged over the cycle. For the average contribution linear scaling with respect to $\bar{p}$ is motivated by assumption of linear elastic behavior valid for small strains. The fluctuation contribution is due to a fluctuation fluid loading that is significant only near the glottis. Instead of scaling with the fluctuation part of the fluid loading which is difficult to measure, the fluctuation displacement $\Delta u_{\mathrm{ml},0}(\vec{X}_{\mathrm{SS}})$ is used. This approach too follows from linear elastic tissue behavior. The square-root dependence of the collision-induced stress on the virtual overclosure is motivated by Hertz theory of elastic contact between two three-dimensional bodies [41]. According to this theory the compressive stress on the surface (referred to as impact stress or contact pressure in voice literature [27, 42, 43, 44, 45, 46, 47, 48, 49]) depends on the square-root of the relative approach of the two bodies in contact. At maximum collision $t = t_{\max,n}$, the impact pressure and the relative approach of the VFs are assumed to be proportional respectively to $\sigma_{H,C0}(\vec{X}_{\mathrm{SS}})$ and $u_{\mathrm{ml},C0}(\vec{X}_{\mathrm{SS}})$.

In [2, 14, 15] stress gradients were considered to drive the interstitial fluid within the VF, under the assumption that it behaves as a poroelastic structure. Darcy's law gives the instantaneous velocity of the interstitial fluid $\vec{q}$ relative to the VF structure as

$$\vec{q} = \frac{k}{\phi^f}\boldsymbol{\nabla}\sigma_H, \tag{20}$$

Copyright © 2013 John Wiley & Sons, Ltd.

DOI: 10.1002/cnm

where the interstitial fluid volume fraction ϕ^f and the permeability k of the poroelastic VF structure fluid are assumed to be homogeneous and time-invariant. The permeability k is additionally considered to be isotropic. Using (20) scaled interstitial fluid velocity contributions are defined corresponding to the scaled hydrostatic stress contributions as

$$\bar{\hat{\vec{q}}}(\vec{X}) \equiv \frac{k}{\phi^f}\boldsymbol{\nabla}\bar{\hat{\sigma}}_H(\vec{X}), \quad \Delta\hat{\vec{q}}(\vec{X},t) \equiv \frac{k}{\phi^f}\boldsymbol{\nabla}\Delta\hat{\sigma}_H(\vec{X},t)$$
$$\text{and} \quad \hat{\vec{q}}_C(\vec{X},t) \equiv \frac{k}{\phi^f}\boldsymbol{\nabla}\hat{\sigma}_{H,C}(\vec{X},t). \tag{21}$$

2.3. *Total Interstitial Fluid Velocity Using Superposition*

Consider an experiment conducted at a particular phonation condition e.g. at a TPD given by $\bar{p}$. The VF superior-surface displacement $u_{\text{ml}}(\vec{X}_{\text{SS}},t)$ can be measured during the experiment. By applying the decomposition step the quantities $\Delta u_{\text{ml},0}(\vec{X}_{\text{SS}})$ and $u_{\text{ml},C0}(\vec{X}_{\text{SS}})$ can be obtained. The total interstitial velocity $\vec{q}$ in that experiment is determined by the weighted sum

$$\vec{q} = \bar{p}\bar{\hat{\vec{q}}}(\vec{X}) + \Delta u_{\text{ml},0}(\vec{X}_{\text{SS}})\Delta\hat{\vec{q}}(\vec{X},t) + \sqrt{u_{\text{ml},C0}(\vec{X}_{\text{SS}})}\hat{\vec{q}}_C(\vec{X},t). \tag{22}$$

3. A WORKING EXAMPLE

The computational model presented in [2] is capable of simulating three-dimensional VF FSI for a realistic set of VF tissue properties and airflow conditions. The model comprises separate definitions for the continuum regions corresponding to the glottal airflow and the pair of VFs, a contact-interaction model for the VFs, and a coupled interaction model between the fluid and structural domains.

The coordinate system origin for both fluid and structural domains is located at the intersection of the mid-coronal plane, the mid-saggital plane and the VF superior surface. Figure 3a shows the geometry of the glottal airflow domain. The inlet and outlet surfaces on the domain boundary are identified. The subglottal airflow pressure is identified with the pressure at the inlet p_{in}. Pressure at the outlet is fixed at 0 Pa (with respect to a reference pressure p_{ref}). The inlet pressure p_{in} is ramped smoothly from time $t = 0$ to $t = t_{\text{ramp}} = 0.15$ s. In this duration p_{in} increases from zero to $p_{\max} = 400$ Pa. The inlet pressure is held fixed for $t > t_{\text{ramp}}$ implying that $\bar{p} = p_{\max}$ for all computed vibration cycles. No-slip and no-penetration conditions are defined on all bounding surfaces of the fluid domain except the inlet and outlet. Laminar, incompressible flow conditions are assumed, and properties of air at standard temperature and pressure are imposed (table I). Note that the difference between the inlet and outlet pressures, i.e. the TPD, is identical to the inlet pressure itself.

Figure 3b shows the left VF; the right VF has identical geometry. Medial–lateral displacements on the left VF are negative when it is moving away from the right VF, and positive when approaching it. Specific dimensions of the VF volumes appear in table II. The geometry of both VFs follows the M5 specification as considered in [50]. The two-dimensional (2D) VF shape pertaining to the M5 definition is extruded uniformly through the length L of the VF in the anterior–posterior direction. The initial (pre-phonatory) separation between the VFs is $d_g = 0.600$ mm. The lateral, anterior and posterior surfaces are fixed. Linear viscoelastic tissue properties are assumed, motivated by the biphasic description of VF tissue in [15]. The viscoelastic properties imposed table II correspond to a fluid volume fraction $\phi^f = 0.7$ and hydraulic permeability $k = 4.05 \times 10^{-8}$ m^2/Pa·s; these biphasic tissue conditions were shown [2] to be representative of a well-hydrated VF tissue.

A pair of rigid planes (P_L and P_R) is situated symmetrically between the VFs (figure 4). The planes are oriented parallel to each other, with a separation of $d_p = 0.200$ mm between them. The rigid planes remain static throughout the computation. Contact interaction is defined between corresponding contact-prone regions of the VF surface and the static rigid planes, i.e. between C_L on the left VF and P_L, and between C_R on the right VF and P_R. Hard, frictionless contact conditions are enforced using penalty methods. The constitutive model for contact ensures that locations on the VF surface are stress-free unless they are in contact, in which compressive normal tractions exist at those locations. This contact model allows the fluid volume between the VFs to have a constant topology throughout the computation, a requirement of the numerical solver used herein.

The time-integration of the fluid and solid domains proceeds in a staggerred manner. At the end of each computed time increment ($\Delta t = 10\ \mu$s), the flow solver communicates the pressures on the VF surfaces to the solid domain solver. The solid domain solver interprets the pressures as tractions, computes the VF deformation under the loading imposed by these tractions over an equal increment of time Δt, and communicates back the displaced VF surface coordinates to the flow solver. The flow solver interprets the modified VF surface coordinates as a moving boundary problem, remeshes the flow domain, and the cycle repeats itself. Details of the governing equations, discretization and solution algorithms are provided in [2].

4. RESULTS

In applying the decomposition and scaling steps, a choice of superior-surface location $\vec{X}_{\mathrm{SS}}$ is necessary. In the example computation, the location $\vec{X}_{\mathrm{SS}} = (0.00, -1.86, 0.00)$ mm was selected (figure 5). This location lies on the mid-coronal plane. This choice was motivated by the observation that collision was significant at the mid-coronal plane [2]. Thereby collision-induced effects on interstitial flow are expected to be significant at the mid-coronal plane. Based on the graph of $u_{\mathrm{ml}}(\vec{X}_{\mathrm{SS}}, t)$ the maximum open instants are obtained, which in turn lead to the identification of individual vibration cycles (cycle numbers indicated in table III). The average cycle period t_p was found to be 0.00597 s with a standard deviation (SD) of 5.70×10^{-5} s (less than 1% of average). A total of 16 cycles were identified. Note that cycle 1 is the first well-developed periodic vibration cycle. In the ramp phase i.e. from $t = 0$ s to $t = 0.15$ s $(= t_{\mathrm{ramp}})$ the motion of $\vec{X}_{\mathrm{SS}}$ is quasi-static and from $t = 0.15$ s to $t = 0.19$ s the vibration pattern is transient in nature. Since quasi-static and transient motion regimes are not the focus of this study these are omitted in the rest of the paper.

Substantial contact at the mid-coronal section is found to occur at $\vec{X}_{\mathrm{C}} = (-0.740, -0.294, 0.00)$ mm. This point lies at the medial extremity of the left VF at mid-coronal section (figure 5). Figure 6 shows the contact opening at $\vec{X}_{\mathrm{C}}$ (i.e. its distance from plane P_L) for all 16 vibration cycles. After the collision-free cycles 1–9, the left VF was predicted to vibrate with an amplitude large enough to induce contact (cycle 10 onward). In cycles 10–16, time intervals are given in table III during which $\vec{X}_{\mathrm{C}}$ sustains compressive normal tractions.

Copyright © 2013 John Wiley & Sons, Ltd.
Prepared using cnmauth.cls

4.1. *Decomposition of Superior-Surface Displacement and Hydrostatic Stress*

For cycle 9, it was determined that $\bar{u}_{\text{ml}}(\vec{X}_{\text{SS}}) = -0.108$ mm, and $\Delta u_{\text{ml},0}(\vec{X}_{\text{SS}}) = -0.260$ mm. Further, the time-variation $f(t)$ and $\bar{t} = 0.23936$ s were also determined. For cycles 10–16, the initial guesses for collision intervals are indicated in table III. In order that collision-induced effects are reliably determined, it is necessary that contact was 'well-established'. In the following, contact was considered to be well-established if $u_{\text{ml,C0}}(\vec{X}_{\text{SS}})$ was more than 3 % of $|\Delta u_{\text{ml},0}(\vec{X}_{\text{SS}})|$. Hence cycles 10–12 are ignored. Following the determination of $u_{\text{ml},v}(\vec{X}_{\text{SS}}, t)$, final estimates of collision intervals are obtained by locating the largest continuous interval within each cycle in which $u_{\text{ml},C}(\vec{X}_{\text{SS}}, t) < -0.005$ mm. These estimates are $[0.26468, 0.26488]$ s, $[0.27082, 0.27098]$ s, $[0.27640, 0.27682]$ s and $[0.28230, 0.28314]$ s respectively for cycles 13–16. Following the 3 % rule above, only cycles 15 and 16 are analyzed. In figure 8, the displacement $u_{\text{ml}}(\vec{X}_{\text{C}}, t)$ is compared with $u_{\text{ml},v}(\vec{X}_{\text{C}}, t)$ in cycles 15 and 16. The temporal variation $g(\tilde{t})$ for cycles 15 and 16 are compared in Appendix A.

Following the decomposition of displacement in the collision-free vibration cycle contours of instantaneous hydrostatic stress $\sigma_H(\vec{X}, t_9)$ i.e. at the maximum open instant of cycle 9 are plotted (figure 7a) on the left VF mid-coronal plane. Figures 7b and 7c show contours of $\bar{\sigma}_H(\vec{X})$ and $\Delta\sigma_{H,0}(\vec{X})$ respectively for cycle 9. Results are presented only for the mid-coronal plane because the components of the hydrostatic stress gradient (and also the interstitial flow driven by it) were found to be much larger along the mid-coronal plane than in the out-of-plane direction [2].

The collision intervals estimated above are used in determining collision-induced stresses. In cycle 15, the collision-induced hydrostatic stress $\sigma_{H,C}(\vec{X}, t)$ is determined. At three indicative instants within the collision interval, $\sigma_H(\vec{X}, t)$ contours on the mid-coronal plane are shown in figure 9a–c, simultaneously with the respective $\sigma_{H,C}$ contours in figure 9d–f. At $t = 0.27640$ s, $\sigma_{H,C}$ in the neighbourhood of $\vec{X}_{\text{C}}$ is only weakly compressive. At $t = t_{\max,15} = 0.27662$ s (figure 9e) the compressive hydrostatic stress increases by a factor greater than 2.5, reaching a maximum over the collision interval. This is followed by a decay until $t = 0.27680$ s (figure 9f).

4.2. *Scaling Hydrostatic Stress and Interstitial Fluid Velocity Contributions*

By using (19) the scaled contributions to hydrostatic stress are obtained in both cycle 9 and 15. Next by using (21) scaled contributions to the interstitial fluid velocity is obtained as a function of spatial location and time in cycles 9 and 15. As mentioned above the anterior–posterior gradient of hydrostatic stress is a small fraction of the total magnitude of the gradient. Hence for the remainder of the analysis the anterior–posterior component is neglected for all hydrostatic stress gradient contributions. Next, the computed field $\boldsymbol{\nabla}\Delta\hat{\sigma}_{H,0}$ in cycle 9 is averaged over the area of the mid-coronal plane in the region $X_{\text{ml}} > -6.67$ mm (bounded on the left by the dashed line in figure 5). Unit vectors $\vec{e}_1$ and $\vec{e}_2$ are defined as respectively perpendicular and parallel to this average gradient. A location $\vec{X}_{\text{I}}$ is selected in the VF interior such that the vector $\vec{X}_{\text{C}} - \vec{X}_{\text{I}}$ is parallel to $\vec{e}_1$. In the results to follow $d \equiv \|\vec{X}_{\text{C}} - \vec{X}_{\text{I}}\| = 4.63$ mm is the depth of VF tissue along $\vec{e}_1$ for which interstitial flow is analysed. The origin of a 2D coordinate system is defined at $\vec{X}_{\text{I}}$; the coordinate system is obtained by a Euclidean transformation of the original $X_{\text{is}}, X_{\text{ml}}$ coordinates. The new coordinate system ξ_1, ξ_2 has axes parallel to $\vec{e}_1$ and $\vec{e}_2$ respectively. The location $(d, 0)$ in the new coordinates corresponds to $\vec{X} = \vec{X}_{\text{C}}$. Locations $\vec{X}_{\text{Up}}$ and $\vec{X}_{\text{Dn}}$ are identified at the intersection of the

Copyright © 2013 John Wiley & Sons, Ltd.

$\vec{e}_2$-axis with, respectively, the superior and inferior VF surfaces (figure 5). All the reference-points are given in table IV in the original coordinate system. Based on the new coordinate system the following quantities are assumed to be zero: $\partial\bar{\hat{\sigma}}_H/\partial\xi_2$, $\partial\hat{\sigma}_{H,C0}/\partial\xi_2$, $\partial\Delta\hat{\sigma}_{H,0}/\partial\xi_1$, $\partial^2\bar{\hat{\sigma}}_H/\partial\xi_1\partial\xi_2$, $\partial^2\hat{\sigma}_{H,C0}/\partial\xi_1\partial\xi_2$ and $\partial^2\Delta\hat{\sigma}_{H,0}/\partial\xi_1\partial\xi_2$. The above simplifications allow determining in closed-form the spatio-temporal variation of the scaled contributions to $\vec{q}$ as follows.

Figure 10a shows the variation of $\bar{\sigma}_H$ with respect to ξ_1. A linear approximation to the derivative $\partial\bar{\hat{\sigma}}_H/\partial\xi_1$ is found to be correct to $r = 0.997$. The coefficients a_1 and a_2 in

$$\bar{\hat{\vec{q}}} \simeq \frac{k}{\phi^f}\frac{\partial\bar{\hat{\sigma}}_H}{\partial\xi_1}\vec{e}_1 \simeq (a_1\xi_1 + a_2)\vec{e}_1, \tag{23}$$

appear in table V. Figure 10b shows the variation of $\Delta\sigma_{H,0}$ with respect to ξ_2. Approximating $\partial\Delta\hat{\sigma}_{H,0}/\partial\xi_2$ with a constant yields $r = 0.999$, and the coefficient b_1 in

$$\Delta\hat{\vec{q}} \simeq \frac{k}{\phi^f}\frac{\partial\Delta\hat{\sigma}_{H,0}}{\partial\xi_2}f(t)\vec{e}_2 \simeq b_1 f(t)\vec{e}_2, \tag{24}$$

is given in table V.

Figure 11 plots $\sigma_{H,C}$ along ξ_1 at 6 equally spaced instants in cycle 15. At the instant of maximum collision $t = t_{\mathrm{max},15}$, the value at the surface of the collision-induced hydrostatic stress is related to the coefficients

$$c_2 \equiv \left(\frac{k}{\phi^f}\right)\hat{\sigma}_{H,C0}(\vec{X}_{\mathrm{C}}), \tag{25}$$

and the gradient of the stress at the surface in the $\vec{e}_1$-direction is related to the coefficient

$$c_1 \equiv \frac{k}{\phi^f}\left.\frac{\partial\hat{\sigma}_{H,C0}}{\partial\xi_1}\right|_{\vec{X}=\vec{X}_{\mathrm{C}}}. \tag{26}$$

The values of c_1 and c_2 are given in table V. Motivated by Hertz theory as earlier, it is assumed that $\sigma_{H,C}(\vec{X}_{\mathrm{C}}, t) \propto \sqrt{g(\tilde{t})}, \quad \forall t \in [t_{c,n}, t_{o,n}]$. A modified Heaviside operator is defined

$$H^*(\xi_1, \tilde{t}) \equiv H\left[\xi_1 - d + (c_2/c_1)\sqrt{g(\tilde{t})}\right], \tag{27}$$

such that it is zero below a time-varying 'collision-influence depth' $(c_2/c_1)\sqrt{g(\tilde{t})}$ measured from $\vec{X}_{\mathrm{C}}$ (in the $\vec{e}_1$-direction). At each of the above 6 time instants a constant-slope approximation to $\hat{\sigma}_{H,C}$ in dependence of ξ_1 is found correct to $r \geq 0.936$ in the region where $H^* = 1$. Outside this region, the gradients of collision-induced hydrostatic stress are small: on average, these are less than 8% of the constant gradient at the medial surface. These results motivate the approximation

$$\hat{\vec{q}}_C \simeq \frac{k}{\phi^f}\frac{\partial\hat{\sigma}_{H,C}}{\partial\xi_1}\vec{e}_1 \simeq c_1 H^*(\xi_1, \tilde{t})\vec{e}_1. \tag{28}$$

4.3. *Phonation Condition Dependent Systemic Hydration*

In the following, total interstitial fluid velocity $\vec{q}$ is computed using (22) for a range of phonation conditions. Each phonation condition is parameterized by the factors $\bar{p}$, $\Delta u_{\mathrm{ml},0}(\vec{X}_{\mathrm{SS}})$ and $u_{\mathrm{ml},C0}(\vec{X}_{\mathrm{SS}})$ each of which can be measured during an experiment at that condition. However, in the absence of available experiments representative values of phonation condition parameters are considered (table VI). Note that $\bar{p} = 1000$ Pa is characteristic of the experimental airflow conditions in [51, 52, 46]. Assuming that $\bar{u}_{\mathrm{ml}}(\vec{X}_{\mathrm{SS}})$ and $\bar{p}$ scale linearly (see Appendix B), and using $\bar{u}_{\mathrm{ml}}(\vec{X}_{\mathrm{SS}}) = -0.116$ mm from cycle 15 in the example computation ($\bar{p} = 400$ Pa), one predicts $\bar{u}_{\mathrm{ml}}(\vec{X}_{\mathrm{SS}}) = -0.290$ mm at $\bar{p} = 1000$ Pa. The choice of $\Delta u_{\mathrm{ml},0}(\vec{X}_{\mathrm{SS}})$ and $u_{\mathrm{ml},C0}(\vec{X}_{\mathrm{SS}})$ values is motivated as follows. In the computation the initial contact separation at $\vec{X}_{\mathrm{C}}$ is its distance from the plane P_L, whereas in the experimental model the distance between $\vec{X}_{\mathrm{C}}$ on the left VF and the corresponding point on the right VF must be considered as the initial contact separation. In either case, the initial contact separation limits the displacement in the medial direction. For e.g. in the computation,

$$u_{\mathrm{ml}}(\vec{X}_{\mathrm{C}}, t) \leq (d_g - d_p)/2. \tag{29}$$

For small strains this relationship extends to $\vec{X}_{\mathrm{SS}}$, which when rearranged implies

$$-u_{\mathrm{ml},C0}(\vec{X}_{\mathrm{SS}}) \simeq (d_g - d_p)/2 - \left[\bar{u}_{\mathrm{ml}}(\vec{X}_{\mathrm{SS}}) + \Delta u_{\mathrm{ml},0}(\vec{X}_{\mathrm{SS}}) f(t_{\max})\right]. \tag{30}$$

Using functions f and g, as obtained from the computed cycle 15 above, in (30) it is predicted that marginal contact occurs at $\Delta u_{\mathrm{ml},0}(\vec{X}_{\mathrm{SS}}) = -0.490$ mm. Thus in table VI cases 1–3 correspond to, respectively, no contact, marginal contact and significant contact. In the marginal contact case 2, no collision-induced stresses are developed. In case 3, it is assumed that the maximum overclosure $u_{\mathrm{ml},C0}(\vec{X}_{\mathrm{SS}})$ is identical to the difference of $\Delta u_{\mathrm{ml},0}(\vec{X}_{\mathrm{SS}})$ between cases 2 and 3, and $t_c = t_n + 0.00209$ s and $t_o = t_n + 0.00370$ s.

Below the trajectories of fluid particles over a vibration cycle are analyzed in dependence of their initial location on the VF mid-coronal plane for each of the three phonation conditions. In particular, five interstitial fluid particles are considered located initially (i.e. at a particular maximum open instant t_n) at equal intervals along the ξ_1 axis (starting at $\xi_1 = 2.50$ mm and ending at $\xi_1 = 4.50$ mm).

Figure 12 shows the interstitial fluid particle trajectories for the cases considered. In case 1 (figure 12a), net movement of fluid particles towards the medial surface ($\xi_1 = d$) is higher for particles initially closer to the surface. In comparison, the range of displacement in the $\vec{e}_2$-direction is constant (~ 0.010 mm) for all five particles. In case 2 (figure 12b) the range of motion in the $\vec{e}_2$-direction increases uniformly for each particle when compared to that in case 1, but the motion in the ξ_1 direction is unchanged. Figure 12c shows that in case 3 the range of $\vec{e}_2$-motion further increases compared to cases 1 and 2. However the $\vec{e}_1$-motion is modified in a non-trivial manner. For fluid particles released at $\xi_1 = 4.00$ and 4.50 mm, the movement towards the medial surface is set back during the collision interval, resulting in a decrease in net displacement compared to cases 1 and 2. This collision-induced decrease is larger for the particle released at $\xi_1 = 4.50$ mm.

The above results indicate that the effects on hydration of both the average and the collision-induced hydrostatic stress gradient are highest at the medial surface location $\xi_1 = d, \xi_1 = 0$, although these effects counteract each other. Since, the fluctuation contribution sums to zero over a cycle and cannot lead to net displacement, the influence on hydration due to hydrostatic stress gradients is best analyzed at the medial surface. Specifically the influence on hydration is measured

Copyright © 2013 John Wiley & Sons, Ltd.

DOI: 10.1002/cnm

by the displacement quantity

$$U^{\text{if}} \equiv \int_{t_n}^{t_{n+1}} \vec{q} \cdot \vec{e}_1 \mathrm{d}t, \tag{31}$$

which is the per-cycle advance along ξ_1 of an interstitial fluid particle located initially (i.e. at $t = t_n$) at $(\xi_1, \xi_2) = (d, 0)$.

The variation of U^{if} is analyzed in dependence of phonation condition, and this is referred to as the hydration map. In the previous analysis comparing three phonation conditions, it was shown that the parameter $u_{\text{ml,C0}}(\vec{X}_{\text{SS}})$ was dependent on $\bar{p}$ and $\Delta u_{\text{ml},0}(\vec{X}_{\text{SS}})$ for the given VF geometry. Thus the dependence of U^{if} on $u_{\text{ml,C0}}(\vec{X}_{\text{SS}})$ is already included in the hydration map. In figure 13 contours of U^{if} in dependence of $\bar{p}$ and $\Delta u_{\text{ml},0}(\vec{X}_{\text{SS}})$ are plotted. For a given combination of parameters, a negative value of $u_{\text{ml,C0}}(\vec{X}_{\text{SS}})$ determined from (30) indicates an absence of collision. Such parameter combinations lie above the dashed curve in figure 13 that represents marginal contact $u_{\text{ml},C0}(\vec{X}_{\text{SS}}) = 0$, and is in fact a straight line. The solid curve in figure 13 represents marginal per-cycle advance of interstitial fluid i.e. $U^{\text{if}} = 0$. Along this curve, the setback in the flow due to collision matches the forward motion due to the average stress gradient. For airflow conditions below this curve, collision causes fluid to be removed from near-surface regions in each cycle (i.e. $U^{\text{if}} < 0$).

5. DISCUSSION

To determine the total interstitial fluid velocity during VF vibration and collision using (21) an important prerequisite is that the medial–lateral displacement of a superior surface location $\vec{X}_{\text{SS}}$ be accessible to high-speed imaging. *A priori* selection of $\vec{X}_{\text{SS}}$ is governed by two conditions: accessibility to imaging during vibration without and with collision, as well as sufficient proximity to the medial surface. Using established imaging procedures [53, 54, 46] the medial–lateral motion of the superior-surface point is easily tracked in a clinical setting. On the other hand, proximity to the medial surface ensures that the collision-induced medial–lateral displacement at $\vec{X}_{\text{SS}}$ will be sufficiently larger than the uncertainty in displacement measurement at that point. This is important because, as was shown in this paper, the influence of collision is not negligible only in the vicinity of the medial surface.

A significant advantage in using (21) to determine interstitial fluid velocity is that the problem of quantifying systemic hydration is much simplified. The equation requires the input of hydration coefficients (table V) that approximate the spatial distribution of the decomposed (and scaled) contributions to interstitial fluid velocity within the VF. These parameters depend only on VF tissue properties, VF geometry and initial VF configuration, but are invariant with respect to phonation-condition parameters e.g. flow pressure and vibration amplitude. Hence a single FSI computation as performed in [2] suffices to determine systemic hydration over a range of phonation conditions. Indeed the main goal of this study, i.e. determining the hydration map, hinges on finding the set of hydration coefficients.

The sense of the scaled average interstitial fluid velocity along $\vec{e}_1$, as determined from (23) and table V, dictates that interstitial fluid is driven from the interior to the medial surface of the VFs. With regard to scaling, the assumption of linear scaling between the average hydrostatic stress and

Copyright © 2013 John Wiley & Sons, Ltd.

DOI: 10.1002/cnm

the TPD is validated in appendix B. Increasing the average TPD therefore increases the strength of average interstitial flow. Moreover the velocity increases as the medial surface approaches. In particular, one finds that the average interstitial fluid velocity in the $\vec{e}_1$ direction at $\xi_1 = 0$ is 18.3 times smaller compared to that at $\xi_1 = d$. This finding of negligible interstitial fluid velocity at $\xi_1 = 0$ is taken as *a posteriori* justification for the choice of depth $d = 4.63$ mm considered for interstitial flow analysis in the case of the model in [2].

The distribution of the fluctuation contribution to hydrostatic stress on the reference mid-coronal plane was found to have an average gradient at an angle of $\sim 25°$ to the vertical (direction $\vec{e}_2$). The nearly linear variation of fluctuation hydrostatic stress with ξ_2 follows the flexural stress distribution in a beam with respect to distance from the neutral axis. Fluctuation contribution to hydrostatic stress alters in sense with the fluctuation in VF displacement about its average value. During the open phase, the fluctuation stress distribution is such that it aids the flow towards the inferior regions. Correspondingly, in the closed phase, the stresses direct the interstitial fluid to the superior surface. In the $\vec{e}_2$ direction the range of per-cycle interstitial fluid motion was found to be $O(0.060\ \mathrm{mm})$ for the range of $\Delta u_{\mathrm{ml},0}(\vec{X}_{\mathrm{SS}})$ considered in figure 13. The mean thickness of the lamina propria, the region of VF tissue which actively vibrates during phonation, is ~ 1.25 mm [55]. Thus the per-cycle interstitial fluid displacement is typically two orders of magnitude smaller than the total thickness of the lamina propria. However, the individual layers of the lamina propria are $O(0.500\ \mathrm{mm})$ thick [55]. Thus, within these individual layers the fluctuation-induced interstitial fluid velocity is expected to play a significant and beneficial role in circulating interstitial fluid. However, the fluctuation-induced interstitial fluid velocity does not contribute in net increase or decrease of hydration in a region of VF tissue. The fluctuation contributions to stresses and displacement are assumed to be related linearly; this assumption is verified in Appendix B. The distribution of average and fluctuation stresses strongly indicate that in the absence of collision, phonation plays a conducive role towards increasing hydration in the VF tissue.

The collision-induced contribution to hydrostatic stress is active only during the collision interval in a vibration cycle. Throughout the collision interval, the dominant direction of collision-induced interstitial flow was found to be opposed to that of the average interstitial flow. Further, the collision-induced interstitial velocity remains constant within a collision influence depth below the medial surface. The collision-induced interstitial fluid velocity further below the collision influence depth was found to be negligible. The time-dependence of the influence depth follows that of the collision-induced hydrostatic stress at the surface. The peak collision-induced hydrostatic stress is assumed to be proportional to square-root of the virtual overclosure, and the time-dependence of the collision-induced hydrostatic stress is assumed to be self-similar when scaled by the length of the collision interval. These assumptions are validated in Appendix B.

With advancement of computational power, several recent studies have focused on the prediction of VF stresses in the interior arising due to self-sustained oscillations [8, 11, 12]. However, these studies did not make a detailed description of spatial and temporal variations of the hydrostatic stress as carried out in the present study. In [8] a plane stress state was assumed with the anterior–posterior direction being stress free, and the components of the plane stress tensor were determined at several locations along a path similar to $\vec{e}_1$ in this paper. The gradient along $\vec{e}_1$ of the peak-to-peak part of in-plane normal stresses is similar to $\nabla(2\Delta\sigma_{H,0} - \sigma_{H,C0}) \cdot \vec{e}_1$ in the present paper. It was found in [8] that this gradient is significantly larger near the surface than in the interior, thus agree with the

Copyright © 2013 John Wiley & Sons, Ltd.
Prepared using cnmauth.cls

present finding that $\nabla(2\Delta\sigma_{H,0})\cdot\vec{e}_1$ is negligible and $\nabla\sigma_{H,C0}\cdot\vec{e}_1 \propto c_1$ during collision provides a very large stress gradient. The study in [8] also find that the peak-to-peak part of in-plane normal stresses at $\vec{X}_{\mathrm{C}}$ increases with increase in lung pressure (similar to subglottal pressure p_{in} in this paper). Since $\Delta\sigma_{H,0}$ is negligible at $\vec{X}_{\mathrm{C}}$, the rise in peak-to-peak amplitude is dictated by the rise in magnitude of $\sigma_{H,C0}$. This finding agrees with the present understanding of Titze's curve: a higher subglottal pressure leads to a higher collision-induced stress contribution.

An assumption in the analysis presented in this paper is that the time-variation at all locations and for all the following quantities, namely displacements, stresses, stress-gradients and interstitial flow velocities can be approximated by $f(t)$, or the time variation derived from $u_{\mathrm{ml}}(\vec{X}_{\mathrm{SS}}, t)$. Although this assumption is difficult to validate for quantities other than displacements, some support is obtained from the good match between $u_{\mathrm{ml},v}$ and u_{ml} at $\vec{X}_{\mathrm{C}}$ outside collision interval (figure 8).

In figure 13, for the range of phonation condition parameters considered the magnitude of U^{if} was found to be $O(0.500\ \mathrm{mm})$ and corresponded mainly to the sense of dehydrating flow. This level of per-cycle near-surface dehydration is expected to significantly influence the health of the lamina propria. Figure 14 shows the schematic of a typical hydration map. Salient features of the computed hydration map that were observed in figure 13 are indicated in the schematic. In particular, the contours of constant U^{if}, the line of marginal collision and the curve of marginal interstitial fluid advance are shown. General directions of positive and negative trends in U^{if} are indicated. The hatched region between the isolines $u_{\mathrm{ml},C0} = 0$ and $U^{\mathrm{if}} = 0$ comprises flow conditions where contact occurs, yet over a vibration cycle interstitial fluid moves from the interior to the medial surface.

However a further consideration reveals that the two phonation-condition related parameters $\bar{p}$ and $\Delta u_{\mathrm{ml},0}(\vec{X}_{\mathrm{SS}})$ can not be set independently of each other. In [22], Titze suggested an empirical relationship $\Delta Q_{\mathrm{air}} = k_l(\bar{p} - p_{\mathrm{Th}})/p_{\mathrm{Th}}$ where ΔQ_{air} is the fluctuation component of the glottal airflow rate, $k_l > 0$ is a subject-specific constant (units of flow-rate) and p_{Th} is the phonation threshold pressure (PTP), i.e. the lowest TPD at which self-oscillation is sustained. Since a larger VF opening (or more negative $\Delta u_{\mathrm{ml},0}(\vec{X}_{\mathrm{SS}})$) will lead to a larger glottal airflow (more positive ΔQ_{air}), one may postulate that $\Delta u_{\mathrm{ml},0}(\vec{X}_{\mathrm{SS}}) \propto -\Delta Q_{\mathrm{air}}$. This is indeed supported by the experiments of [56] as well as the present computation [2]. Thus Titze's empirical relationship [22] leads to the conclusion that the fluctuation amplitude becomes more negative as $\bar{p}$ increases

$$\Delta u_{\mathrm{ml},0}(\vec{X}_{\mathrm{SS}}) = -k_l(\bar{p} - p_{\mathrm{Th}})/p_{\mathrm{Th}}. \tag{32}$$

In the spirit of [22] the negatively-sloped line of $\Delta u_{\mathrm{ml},0}(\vec{X}_{\mathrm{SS}})$–$\bar{p}$ is referred to as Titze's line. It represents a locus of physically realizable airflow conditions and is shown in figure 14. In the absence of experimental measurements on the example VF model considered in this paper, only a qualitative determination of Titze's line is possible. Nonetheless, some biomechanically relevant landmarks on Titze's line are evident in figure 14.

Titze's line starts at a positive value of p_{Th}. As mentioned above, the slope of Titze's line (32) is always negative. It is expected that Titze's line intersects the marginal collision line at a higher TPD given by $\bar{p} = p_C$ (referred to as collision threshold pressure CTP in voice literature [57]). A variety of subjects comprising professional singers and non-singers were considered in [58]. From their data it can be inferred that the slope of Titze's line is proportional to k_1 in [58] and

Copyright © 2013 John Wiley & Sons, Ltd.
Prepared using cnmauth.cls

for tenors the slope is 66.7 times compared to female non-singers. The marginal collision line is also expected to vary across subjects. Thereby it is expected that p_C also varies significantly across subjects. Figure 14 suggests that there exists a $p_{\rm Safe}$ such that for all $\bar{p} \in (p_C, p_{\rm Safe})$ the VFs undergo collision but without net removal of interstitial fluid from the surface. Thus for this range of pressures (above CTP through $p_{\rm Safe}$) the hydration at near-surface locations is not adverse even in the presence of collision. It is emphasized that the determination of $p_{\rm Safe}$ is possible only if the hydration coefficients in table V are known. The segment of Titze's line that lies above the $U^{\rm if} = 0$ isoline represents conditions that are detrimental to hydration in the near-surface region. Since vocal intensity is a function of the variables $\bar{p}$ and $\Delta u_{{\rm ml},0}(\vec{X}_{\rm SS})$ [58], figure 13 overlaid by Titze's line can provide subject-specific insight into systemic hydration as a function of vocal intensity. It is interesting to note that figure 14 suggests that there exists a $p_{\rm Peak} \in (p_{\rm Safe}, \infty)$ for which interstitial fluid removal per cycle from the VF surface reaches a peak value.

5.1. Limitations

The present approach is underpinned by the principle of linear superposition. While this assumption enables us to construct the hydration map, the assumption of linear superposition will provide only first order results. Future, higher order results are needed if one accounts for the fact that laryngeal tissues possess a nonlinear deformation response.

The two conditions for the selection of $\vec{X}_{\rm SS}$ mentioned above are somewhat counteractive. This is because it becomes increasingly difficult to acquire images as one approaches the medial surface. In this paper, the choice of $\vec{X}_{\rm SS}$ respects typical limitations of image acquisition in an experimental setting [46]. As contact is best judged from displacement of the medial surface, the use of $u_{\rm ml}$ at $\vec{X}_{\rm SS}$ is expected to introduced some errors in quantifying the effect of collision. Indeed, the collision intervals in cycles 13–16 estimated from $u_{\rm ml}(\vec{X}_{\rm SS}, t)$ were always found to be smaller than the computed collision intervals at $\vec{X}_{\rm C}$ given in table III. The resulting underestimation of the collision-interval is because the influence of collision is 'felt' at $\vec{X}_{\rm SS}$ only when the actual collision-influence depth grows sufficiently large to include $\vec{X}_{\rm SS}$. Both these errors are expected to diminish relatively as the severity of collision increases. Note that increase in the severity of collision is accompanied by the decrease in the open-quotient OQ which in terms of the present variables is $OQ = 1 - (t_{o,n} - t_{c,n})/t_p$. The minimum computed OQ considering $u_{\rm ml}(\vec{X}_{\rm C}, t)$ in cycles 13–16 is 0.876, and that estimated from $u_{\rm ml}(\vec{X}_{\rm SS}, t)$ is 0.859. These indicate much milder collision when compared to the experiments conducted in [59] with human subjects where OQ as low as 0.400 were recorded in singing.

Another potential cause of underestimating the collision interval is that the limits of the collision interval are defined when $u_{{\rm ml},C}(\vec{X}_{\rm SS}, t)$ crosses -0.005 mm. This definition ensures that the collision interval limits are determined robustly. The determination of the theoretical condition $u_{{\rm ml},C}(\vec{X}_{\rm SS}, t) = 0$ is error prone because small differences between $u_{\rm ml}$ and $u_{{\rm ml},v}$ due to interpolation function f can be confused for collision-induced effects.

In obtaining the collision-induced contribution in figures 12 and 13, the virtual overclosure was approximated using (30), where it was assumed that the displacement of the material location $\vec{X}_{\rm SS}$ remains constant throughout the collision-interval. In reality, as borne out in both experiments [46] and computation [2] $\vec{X}_{\rm SS}$ displaces further in the medial-direction during the collision-interval. Thus (30) overestimates the virtual overclosure $u_{{\rm ml},C0}(\vec{X}_{\rm SS})$ and the resulting collision influence

Copyright © 2013 John Wiley & Sons, Ltd.

DOI: 10.1002/cnm

depth and dehydration effects are also overestimated. It is emphasized that this overestimation is removable by measuring the true displacement of $\vec{X}_{\mathrm{SS}}$ in a physical experiment corresponding to each phonation condition considered. Moreover, it is expected that the amount of overestimation error in (30) is larger for larger actual values of virtual overclosure; in particular, there is no error in determining when $u_{\mathrm{ml},C0}(\vec{X}_{\mathrm{SS}}) = 0$. It follows that the overestimation will not lead to qualitative changes in figures 12 and 13.

An artifact of the rigid planes in the computation is that corresponding locations on the opposing VFs can have different actual collision intervals. For e.g. in figure 6 the location $\vec{X}_{\mathrm{C}}$ does not undergo collision (zero contact interval) in cycle 8, whereas on a corresponding location on the right VF the actual collision interval is obviously non-zero. This left-right asymmetry does not occur in the absence of the rigid planes and will not influence the determination of interstitial flow in an experimental model.

The underlying basis for (21) is small strain behavior. However during collision, strains can be locally large in magnitude, especially in the collision-influence zone. In cycle 15, at t_{max} the principal strains ranged from -6.50% to 6.50% on the mid-coronal plane and strongly support the linearity assumption. Note that the magnitude of total strain dictates the applicability of (21), and not that of the separate contributions. Along Titze's line, the increasing severity of collision increases the collision-induced strain. However, this is accompanied by an increase in the average strain, which being counteractive to the collision-induced strain, is expected to lower the magnitude of the total strain. Therefore errors introduced due to application of (21) are expected to be maximum at p_{Peak}, and decrease away from it.

The integration of interstitial fluid velocity $\vec{q}$ over sufficiently large time periods should be interpreted with caution. Significant displacement of interstitial fluid can violate the assumption of homogeneous, isotropic, time-invariant distribution of ϕ^{f} and k.

VF tissue is known to possess a layered structure [60] and a non-linear stress–strain response at high strain levels [34, 35, 36]. Thus heterogeneity of response through different VF layers and non-linearity of response in each layer are expected to better characterize the full mechanical behavior of the VF tissue when compared to the linear elastic isotropic response used in the current analysis. However, if the assumption of small strains holds, then resolving the full stress–strain response is not necessary, as deviations due to non-linearity at sufficiently small strains are not significant. The use of a layered model would be interesting but was not considered in this paper. Yet, the method detailed here is applicable in the case of a layered heterogeneous model as well, specifically (i) decomposition of superior surface displacement and hydrostatic stress, and (ii) scaling of contributions to hydrostatic stress and interstitial fluid velocities. Use of a layered model would result in a quantitatively different hydration map than the particular one presented here (figure 13). Although such a modified map might arguably be closer to reality, the main contribution of the present approach is that such a map can be obtained and that biomechanically relevant insights can henceforth be inferred. It is to emphasize this aspect that a qualitative hydration map is presented (figure 14) and the main inferences of this study derive mainly from the qualitative picture.

Anisotropy of apparent stiffness of VF tissue is well known. However, considering VF tissue as a porous material it is not clear whether the anisotropy is intrinsic (the solid phase is an anisotropic material) or structural (porosity of the solid phase is anisotropic). A study of the pore architecture of bovine acellular VF tissue showed that structural anisotropy is not significant and

Copyright © 2013 John Wiley & Sons, Ltd.
Prepared using cnmauth.cls

moreover the medial–lateral permeability (as considered in the present study) is high enough to allow interstitial fluid flow [19]. In an approach similar to ours, interstitial fluid flow in the anterior–posterior direction was assumed negligible by other workers [16, 18] based on the following two observations: (i) the stress gradients in that direction are low even when the VF is intrinsically transversely isotropic and (ii) water flow is dominated by negatively charged non-fibrillar matrix molecules, which are usually distributed isotropically in the VF tissue. From the above arguments isotropic permeability as considered here appears to be a reasonable assumption. On the other hand, while incorporating intrinsic transverse anisotropy is expected to lead to a better prediction of VF hydrostatic stress, the approach detailed in the present paper can without any modification use such a predicted stress state in order to derive VF tissue hydration. The results presented in this paper are expected to only undergo quantitative changes and the final insights drawn are expected to be valid.

It is emphasized that the current study presents a novel approach that derives characteristics of VF hydration as a function of phonation conditions for given VF tissue mechanical properties and VF geometry. This approach is demonstrated using the results from an FSI computation in literature which assumes a particular VF tissue description and VF geometry, but the approach is not limited to these. The actual quantitative description of dehydration characteristics for all possible VF tissue mechanical properties (and VF geometries) is outside the scope of the present study.

6. CONCLUSION

The dominant features of temporal and spatial variation of the interstitial fluid velocity $\vec{q}$ within the VF were investigated in this paper under conditions of VF vibration without and with collision. This result was further extended by introducing the hydration map analysis, wherein a measure of VF hydration i.e. U^{if}, is used to compare the state of VF hydration over a range of phonation conditions. Throughout the paper, it was considered that $\vec{q}$ is solely dependent on the gradient of the hydrostatic stress. Consequently, systemic hydration as considered here is entirely driven by VF vibration. At an arbitrary phonation condition $\vec{q}$ was determined using the hydrostatic stress gradient obtained from a single computation conducted at a specific and distinct phonation condition. This determination was made possible by employing decomposition and scaling of the hydrostatic stress distribution. Additionally, the definition of a virtual function f to extract the collision-induced contribution, and the scaling of the collision-induced stress with the square-root of the displacement are new concepts presented in this paper. The spatiotemporal variation of $\vec{q}$, and in particular the variation of its scaled and decomposed contributions $\bar{\hat{\vec{q}}}$, $\Delta\hat{\vec{q}}$ and $\hat{\vec{q}}_C$ is captured by a set of hydration coefficients given in table V. These coefficients are in turn related to the imposed VF tissue constitutive properties and VF geometry but are independent of phonation conditions. It is emphasized that at present, the only method available to determine these coefficients is a computation of VF vibration with collision, an example of which is given in [2]. As a consequence, similar computations that exist in literature, as well as those that will be performed in future, can be analyzed in the method described in this paper. The outcome of such an analysis would be the set of hydration coefficients, and the determination of a hydration map. It is expected that in the future it will be possible to include subject-specific VF tissue constitutive properties in numerical simulations of VF vibration. This will lead to subject-specific hydration coefficients and determination of the hydration map will provide a

Copyright © 2013 John Wiley & Sons, Ltd.

DOI: 10.1002/cnm

higher degree of subject-specific insight into the systemic hydration of the VF tissues. A quantitative subject-specific assessment of systemic hydration over a range of phonation conditions is then quite straightforward, provided routine *in vivo* measurements of airflow pressure and VF displacements are obtained. Obtaining these measurements is expected to be much less expensive than conducting a full-scale computational FSI at that particular phonation condition.

REFERENCES

[1] Alipour F, Scherer RC. Flow separation in a computational oscillating vocal fold model. *J. Acoust. Soc. Am.* 2004; **116**(3):1710–1719.

[2] Bhattacharya P, Siegmund T. A computational study of systemic hydration in vocal fold collision. *Comput. Meth. Biomech. Biomed. Eng.* in press; doi:10.1080/10255842.2013.772591.

[3] Decker GZ, Thomson SL. Computational simulations of vocal fold vibration: Bernoulli versus NavierStokes. *J. Voice* 2007; **21**(3):273–284.

[4] Luo H, Mittal R, Zheng X, Bielamowicz SA, Walsh RJ, Hahn JK. An immersed-boundary method for flow-structure interation in biological systems with application to phonation. *J. Comput. Phys.* 2008; **227**:9303–9332.

[5] Luo H, Mittal R, Bielamowicz SA. Analysis of flow-structure interation in the larynx during phonation using an immersed boundary method. *J. Acoust. Soc. Am.* August 2009; **126**(2):816–824.

[6] Mittal R, Zheng X, Bhardwaj R, Seo JH, Xue Q, Bielamowicz S. Toward a simulation-based tool for the treatment of vocal fold paralysis. *Front. Physio.* 2011; **2**:19.

[7] de Oliveira Rosa M, Pereira JC, Grellet M, Alwan A. A contribution to simulating a three-dimensional larynx model using the finite-element model. *J. Acoust. Soc. Am.* November 2003; **114**(5):2893–2905.

[8] Thomson SL, Mongeau L, Frankel SH. Aerodynamic transfer of energy to the vocal folds. *J. Acoust. Soc. Am.* September 2005; **118**(3):1689–1700.

[9] Zheng X, Bielamowicz S, Luo H, Mittal R. A computational study of the effect of false vocal folds on glottal flow and vocal fold vibration during phonation. *Ann. Biomed. Eng.* 2009; **37**(3):625–642.

[10] Zheng X, Xue Q, Mittal R, Bielamowicz SA. A coupled sharp-interface immersed boundary-finite-element method for flow-structure interaction with application to human phonation. *J. Biomech. Eng.* 2010; **132**(11):111 003.

[11] Sivasankar M, Leydon C. The role of hydration in vocal-fold physiology. *Curr. Opin. Otolaryngo.* 2010; **18**(3):171–175.

Copyright © 2013 John Wiley & Sons, Ltd.
Prepared using cnmauth.cls

[12] Simon BR. Multiphase poroelastic finite element models for soft tissue structures. *Appl. Mech. Rev.* 1992; **45**(6):191–218.

[13] Diebels S, Ehlers W. Dynamic analysis of a fully saturated porous medium accounting for geometrical and material non-linearities. *Int. J. Numer. Meth. Eng.* 1996; **39**(1):81–97.

[14] Tao C, Jiang JJ, Zhang Y. A fluid-saturated poroelastic model of the vocal folds with hydrated tissue. *J. Biomech* 2009; **42**(6):774–780.

[15] Zhang Y, Czerwonka L, Tao C, Jiang JJ. A biphasic theory for the viscoelastic behaviors of vocal fold lamina propria in stress relaxation. *J. Acoust. Soc. Am.* 2008; **123**(3):1627–1636.

[16] Heris HK, Miri AK, Tripathy U, Barthelat F, Mongeau L. Indentation of poroviscoelastic vocal fold tissue using an atomic force microscope. *J. Mech. Behav. Biomed. Mat.* 2013; **28**:383–392.

[17] Tao C, Jiang JJ, Czerwonka L. Liquid accumulation in vibrating vocal fold tissue: A simplified model based on a fluid-saturated porous solid theory. *J. Voice* 2010; **24**(3):260–269.

[18] Tao C, Liu XJ. Effects of poroelastic coefficients on normal vibration modes in vocal-fold tissues. *J. Acoust. Soc. Am.* 2011; **129**(2):934–943.

[19] Xu CC, Chan RW. Pore architecture of a bovine acellular vocal fold scaffold. *Tiss. Eng. Pt. A* 2008; **14**(11):1893–1903.

[20] Manfredini P, Cocchetti G, Maier G, Redaelli A, Montevecchi FM. Poroelastic finite element analysis of a bone specimen under cyclic loading. *J. Biomech.* 1999; **32**(2):135–144.

[21] Holmberg EB, Hillman RE, Perkell JS. Glottal airflow and transglottal air pressure measurements for male and female speakers in soft, normal, and loud voice. *J. Acoust. Soc. Am.* 1988; **84**(2):511–529.

[22] Titze IR. Phonation threshold pressure: A missing link in glottal aerodynamics. *J. Acoust. Soc. Am.* 1992; **91**(5):2926–2935.

[23] Sadie S ((ed.)). *The New Grove Dictionary of Music and Musicians*, vol. 6. Grove Dictionaries Inc., 1980.

[24] Alipour F, Scherer RC, Finnegan E. Pressure-flow relationships during phonation as afunction of adduction. *J. Voice* 1997; **11**(2):187 – 194.

[25] Cranen B, Boves L. Pressure measurements during speech production using semiconductor miniature pressure transducers: Impact on models for speech production. *J. Acoust. Soc. Am.* 1985; **77**(4):1543–1551.

[26] Plant RL, Freed GL, Plant RE. Direct measurement of onset and offset phonation threshold pressure in normal subjects. *J. Acoust. Soc. Am.* 2004; **116**(6):3640–3646.

[27] Chen LJ. Investigations of mechanical stresses within human vocal folds during phonation. PhD Thesis, Purdue University 2009.

[28] George NA, de Mul FFM, Qiu Q, Rakhorst G, Schutte HK. New laryngoscope for quantitative high-speed imaging of human vocal folds vibration in the horizontal and vertical direction. *J. Biomed. Opt.* 2008; **13**:064 024.

[29] Kobler JB, Chang EW, Zeitels SM, Yun SH. Dynamic imaging of vocal fold oscillation with four-dimensional optical coherence tomography. *Laryngoscope* 2010; **120**(7):1354–1362.

[30] Larsson H, Hertegard S. Vocal fold dimensions in professional opera singers as measured by means of laser triangulation. *J. Voice* 2008; **22**(6):734–739.

[31] Riede T, York A, Furst S, Muller R, Seelecke S. Elasticity and stress relaxation of a very small vocal fold. *J. Biomech.* 2011; **44**(10):1936–1940.

[32] Backshaei H, Yang J, Miri AK, Mongeau L. Determination of the stresses and strain on the superior surface of excised porcine larynges during phonation using digital image correlation. *Proc. Mtgs. Acoust.*, vol. 19, Acoust. Soc. Am., AIP, 2013; 060 238.

[33] Bakhshaee H, Young J, Yang JCW, Mongeau L, Miri AK. Determination of strain field on the superior surface of excised larynx vocal folds using dic. *J. Voice* 2013; **27**(6):659–667.

[34] Min YB, Titze IR, Alipour-Haghighi F. Stress-strain response of the human vocal ligament. *Ann. Otol. Rhinol. Laryngol.* 1995; **104**:563–569.

[35] Zhang K, Siegmund T, Chan RW. A constitutive model of the human vocal fold cover for fundamental frequency regulation. *J. Acoust. Soc. Am.* 2006; **119**(2):1050–1062.

[36] Kelleher JE, Siegmund T, Chan RW, Henslee EA. Optical measurements of vocal fold tensile properties: Implications for phonatory mechanics. *J. Biomech.* 2011; **44**(9):1729–1734.

[37] Alipour-Haghighi F, Titze IR. Elastic models of vocal fold tissues. *J. Acoust. Soc. Am.* 1991; **90**(3):1326–1331.

[38] Gunter HE. Modeling mechanical stresses as a factor in the etiology of benign vocal fold lesions. *J. Biomech.* 2004; **37**(7):1119–1124.

[39] Tao C, Jiang JJ. Mechanical stress during phonation in a self-oscillating finite-element vocal fold model. *J. Biomech.* 2007; **40**(10):2191–2198.

[40] Deguchi S, Kawahara Y, Takahashi S. Cooperative regulation of vocal fold morphology and stress by the cricothyroid and thyroarytenoid muscles. *J. Voice* 2011; **25**(6):E255–E263.

[41] Timoshenko S, Goodier JN. 2nd edn., McGraw-Hill, 1970.

[42] Chen LJ, Mongeau L. Measurements of the contact pressure in human vocal folds. *EMBC: 2009 Conf. Proc. IEEE Eng. Med. Biol. Soc.*, vol. 1–20, 2009; 869–872.

[43] Horáček J, Laukkanen AM, Šidlof P, , Murphy P, Švec JG. Comparison of accelaration and impact stress as possible loading factors in phonation: a computer modeling study. *Folia Phoniatr.* 2009; **61**(3):137–145.

Copyright © 2013 John Wiley & Sons, Ltd.

Prepared using cnmauth.cls

[44] Jiang JJ, Titze IR. Measurement of vocal fold intraglottal pressure and impact stress. *J. Voice* 1994; **8**(2):132–144.

[45] Jiang JJ, Shah AG, Hess MM, Verdolini K, Banzali FM, Hanson DG. Vocal fold impact stress analysis. *J. Voice* 2001; **15**(1):4–14.

[46] Spencer M, Siegmund T, Mongeau L. Determination of superior-surface strains and stresses, and vocal fold contact pressure in a synthetic larynx model using digital image correlation. *J. Acoust. Soc. Am.* 2006; **123**(2):1089–1103.

[47] Tao C, Jiang JJ, Zhang Y. Simulation of vocal fold impact pressures with a self-oscillating finite-element model. *J. Acoust. Soc. Am.* June 2006; **119**(6):3987–3994.

[48] Verdolini K, Chan R, Titze IR, Hess M, Bierhals W. Correspondence of electroglottographic closed quotient to vocal fold impact stress in excised canine larynges. *J. Voice* 1998; **12**(4):415–423.

[49] Verdolini K, Hess MM, Titze IR, Bierhals W, Gross M. Investigation of vocal fold impact stress in human subjects. *J. Voice* 1999; **13**(2):184–202.

[50] Scherer RC, Shinwari D, DeWitt KJ, Zhang C, Kucinschi BR, Afjeh AA. Intraglottal pressure profiles for a symmetric and oblique glottis with a divergence angle of 10 degrees. *J. Acoust. Soc. Am.* 2001; **109**(4):1616–1630.

[51] Erath BD, Plesniak MW. The occurrence of the Coanda effect in pulsatile flow through static models of the human vocal folds. *J. Acoust. Soc. Am.* 2006; **120**(2):1000–1011.

[52] Scherer RC, Titze IR, Curtis JF. Pressure-flow relationships in two models of the larynx having rectangular glottal shapes. *J. Acoust. Soc. Am.* 1983; **73**(2):668–676.

[53] Baer T. Observation of vocal fold vibration: measurement of excised larynges. *Vocal fold physiology*, Stevens KN, Hirano M (eds.). chap. 10, University of Tokyo Press, 1981; 119–132.

[54] George NA, de Mul FFM, Qiu Q, Rakhorst G, Schutte HK. Depth-kymography: high-speed calibrated 3D imaging of human vocal fold vibration dynamics. *Phys. Med. Biol.* 2008; **53**:2667–2675.

[55] Prades JM, Dumollard JM, Duband S, Timoshenko A, Richard C, Dubois MD, Martin C, Peoc'h M. Lamina propria of the human vocal fold: histomorphometric study of collagen fibers. *Surg. Radiol. Anat.* 2010; **32**(4):377–382.

[56] Granqvist S, Hertegard S, Larsson H, Sundberg J. Simultaneous analysis of vocal fold vibration and transglottal airflow: exploring new experimental setup. *J. Voice* September 2003; **17**(3):319–330.

[57] Enflo L, Sundberg J. Vocal fold collision threshold pressure: An alternative to phonation threshold pressure? *Log. Phon. Vocol.* 2009; **34**(4):210–217.

Copyright © 2013 John Wiley & Sons, Ltd.
Prepared using cnmauth.cls

[58] Titze IR, Sundberg J. Vocal intensity in speakers and singers. *J. Acoust. Soc. Am.* 1992; **91**(5):2936–2946.

[59] Henrich N, d'Alessandro C, Doval B, Castellengo M. Glottal open quotient in singing: Measurements and correlation with laryngeal mechanisms, vocal intensity, and fundamental frequency. *J. Acoust. Soc. Am.* 2005; **117**(3):1417–1430.

[60] Kurita S, Hirano M, Mihashi S, Nakashima T. The layer structure of the vocal fold - age-dependent variations. *Folia Phoniatr.* 1980; **32**(3):210–210.

[61] Hildebrand FB. *Introduction to numerical analysis*. Dover: New York, 1974.

[62] Kundu D. Estimating the parameters of complex valued exponential signals. *Comput. Stat. Data Anal.* 1994; **18**(5):525–534.

[63] Pozrikidis C. *Fluid dynamics at interfaces*, chap. Mutifilm flow down an inclined plane: simulation based on the lubrication approximation and normal-mode decomposition of linear waves. Cambridge University press, 1999; 112–128.

[64] Rothenburg M, Mahshie JJ. Monitoring vocal fold abduction through vocal fold contact area. *J. Speech Hearing Res.* 1988; **31**:338–351.

APPENDIX A. APPROXIMATION OF $u_{\mathrm{ml},v}(\vec{X}_{\mathrm{SS}},t)$ IN THE COLLISION INTERVAL

In determining the collision-induced contribution the virtual function $u_{\mathrm{ml},v}(\vec{X}_{\mathrm{SS}},t)$ must be obtained within the initially guessed collision interval. In this paper, this approximation was based on the modified Prony method [61, 62, 63]. In this method $u_{\mathrm{ml}}(\vec{X}_{\mathrm{SS}},t)$ is sampled at four equispaced instants; each such set of four instants lies either in the closing phase immediately preceding the guessed collision interval, or in the opening phase immediately following it (figure 15a). From the sampled data, two separate approximations are determined corresponding to $u_{\mathrm{ml},v}(\vec{X}_{\mathrm{SS}},t)$ on each side of the collision interval. The minimum envelope of the two extrapolated functions is considered to be the desired approximation to $u_{\mathrm{ml},v}(\vec{X}_{\mathrm{SS}},t)$ within the collision interval (figure 15b).

APPENDIX B. ERROR ANALYSIS

This section details the various errors in the decomposition and scaling methods employed in the paper. Other than these, errors in employing Darcy's law and numerical errors in example computation also contribute to the total error in estimating VF systemic hydration. However, a discussion of the latter two sources of error is provided in [2].

Decomposition of the medial–lateral displacement necessitates an integral over time as given in (2). The error in approximating the integral from discrete data points is a function of interval of data output; in the example computation, this is $\Delta t = 20\ \mu$s. For a cycle time period of $t_p = 0.00597$ s, the relative error in the present calculations due to using the trapezoidal-rule for

Copyright © 2013 John Wiley & Sons, Ltd.

integration is $O((\Delta t/t_p)^2) = O(1.12 \times 10^{-5})$. This is also the estimate of error in determining the fluctuation component. Although only cycles 9 and 15 are used in the text, the average displacement does not differ much across cycles. In cycles 1–$9, 15, 16$, it was found that on average $\bar{u}_{\mathrm{ml}}(\vec{X}_{\mathrm{SS}}) = -0.0995$ mm (SD 0.0111 mm). The fluctuation amplitude increased with time, but very slowly. For cycles 1–9, the standard deviation of $u'_{\mathrm{ml},0}(\vec{X}_{\mathrm{SS}})$ was 0.0146 mm, which is less than 5.66 % of the average value. For each of the cycles 1–8 and 13–16, the function $f(t)$ was found to be strongly correlated with that in cycle 9 ($r > 0.993$) and had a maximum absolute difference less than 0.145 compared with $f(t)$ in cycle 9. Compared to the pure cosine function, the correlation of $f(t)$ was high ($r > 0.994$) and the maximum absolute difference between the functions was less than 0.177. These findings are in line with previous studies [64, 22].

The error in approximating the time-dependence of the fluctuation component by the function $f(t)$, which is obtained solely from $u_{\mathrm{ml}}(\vec{X}_{\mathrm{SS}}, t)$, is considered next. Firstly, two ordered sets $\mathbb{E}_1$ and $\mathbb{E}_2$ are defined, which contain respectively the finite elements intersected by the line joining $\vec{X}_{\mathrm{I}}$ and $\vec{X}_{\mathrm{C}}$ and the finite elements intersected by the line joining $\vec{X}_{\mathrm{Up}}$ and $\vec{X}_{\mathrm{Dn}}$. It was found that at each computed instant in cycle 9, the correlation between computed σ_H and estimated $\bar{\sigma}_H + \Delta\sigma_{H,0} f$ was always more than 0.940 for the region corresponding to element-set $\mathbb{E}_1$. Discarding the instants close to $\bar{t}$ and $\bar{t} + t_p/2$ in cycle 9, where the contribution from the fluctuation is expected to be negligible, it was found that the correlation between the computed and estimated hydrostatic stress was 0.850 or higher for the region corresponding to element-set $\mathbb{E}_2$. The discarded instants where the correlation was lower than 0.850 were in total 10.7% of the cycle time period.

In determining the collision-induced contribution, it is assumed that the function $g(\tilde{t})$ is self-similar. Figure 15a,b compares u_{ml} with $u_{\mathrm{ml},v}$, both taken at $\vec{X}_{\mathrm{SS}}$ in cycles 15 and 16. The figure also indicates the instants outside the respective collision intervals at which f is sampled to apply the modified Prony method. Figure 15c compares the function $g(\tilde{t})$ between cycles 15 and 16.

In the scaling model, the self-similarity of the average hydrostatic stress normalized by the averaged TPD ($p_{\max}$ in the computation) is verified by considering results from a separate computation. In this new computation, the same example computational model is used as described herein, except that $p_{\max} = 800$ Pa and $t_{\mathrm{ramp}} = 0.300$ s. This new computation is stopped at $t = t_{\max}$. Considering instants corresponding to when the inlet pressure equals 200 Pa, 300 Pa, 400 Pa, 500 Pa and 600 Pa, it is found that VF vibrations are negligible (instantaneous kinetic energy was at most 3.01 % of the instantaneous strain energy). At each of these instants, it was found that the correlation between σ_H and $\bar{\sigma}_H$ (cycle 9) was higher than 0.995, when regions comprising element-sets $\mathbb{E}_1$ and $\mathbb{E}_2$ were considered. Further, at each instant, the difference between the values of $\bar{\sigma}_H/p$ and $\hat{\sigma}_H$ (cycle 9) taken at $\vec{X}_{\mathrm{SS}}$ was less than 2.95 %.

For the scaling of the fluctuation contribution, the variable $\Delta\hat{\sigma}_0$ is compared between cycle 9 and the 8 vibration cycles preceding it, considering elements in the set $\mathbb{E}_2$. It is found that the corresponding correlation is always 0.999 or greater. For the scaling of the collision-induced contributions, it is noted that between cycles 15 and 16 c_1 differed by 13.4 %. In figure 11, the correlation r is at least 0.936 between the variation of $\sigma_{H,C}$ with ξ_1 (in the region $H^* = 1$) and a line with slope $c_1\sqrt{u_{\mathrm{ml},C0}}$. Between cycles 15 and 16 the value of c_2, which is the scaled collision-induced stress at $\vec{X}_{\mathrm{C}}$ at the instant of maximum overclosure was found to be differing by 16.0 %.

In determininng interstitial flow velocities for hypothetical phonation conditions, a linear relationship between $\bar{u}_{\mathrm{ml}}(\vec{X}_{\mathrm{SS}})$ and $\bar{p}$ was assumed. However [22] suggests that a more accurate

Copyright © 2013 John Wiley & Sons, Ltd.

DOI: 10.1002/cnm

expression is $\bar{u}_{\mathrm{ml}}(\vec{X}_{\mathrm{SS}}) \propto (k_l/p_{\mathrm{Th}})(\bar{p}-p_{\mathrm{Th}})\cos(\pi \cdot OQ)$ where the open-quotient is given by $OQ = k_2 + (1-k_2)(p_{\mathrm{Th}}/\bar{p})$ with $1 > k_2 > 0$ a non-dimensional subject-specific constant. From the above expressions it can be shown that for $\bar{p}$ marginally larger than p_{Th}, $\partial\bar{u}_{\mathrm{ml}}(\vec{X}_{\mathrm{SS}})/\partial\bar{p}$ is negative and $\partial^2\bar{u}_{\mathrm{ml}}(\vec{X}_{\mathrm{SS}})/\partial\bar{p}^2$ is positive. This non-linear relationship between $\bar{u}_{\mathrm{ml}}(\vec{X}_{\mathrm{SS}})$ and $\bar{p}$ implies that the marginal collision line in figures 13 and 14 bends downward for finite values of $\bar{p}-p_{\mathrm{Th}}$ and quantitative differences in the hydration map will follow. Note that these differences can be removed by direct experimental measurement of $\bar{u}_{\mathrm{ml}}(\vec{X}_{\mathrm{SS}})$. Moreover, the non-linearity in the $\bar{u}_{\mathrm{ml}}(\vec{X}_{\mathrm{SS}})$–$\bar{p}$ relationship does not alter the qualitative inferences made in the text regarding the hydration map.

Copyright © 2013 John Wiley & Sons, Ltd.
Prepared using cnmauth.cls

Table I. Geometric dimensions and constitutive properties of glottal airflow model.

Air-tract Dimensions		Air Properties	
T_{entry}	10.0 mm	p_{ref}	101 kPa
T_{exit}	20.0 mm	ρ_{f}	1.23 kg/m^3
T	10.7 mm	μ	1.79×10^{-4} kg/m·s
W	17.4 mm		

Copyright © 2013 John Wiley & Sons, Ltd.
Prepared using cnmauth.cls

Table II. Geometric dimensions and constitutive properties of the vocal fold model.

Vocal Fold Dimensions		Tissue Properties	
L	20.0 mm	E	6.00 kPa
D	8.40 mm	ν	0.450
T	10.7 mm	ρ_{s}	1070 kg/m^3
d_{g}	0.600 mm	τ_1	0.500 s
d_{p}	0.200 mm	k_1, g_1	0.670

Copyright © 2013 John Wiley & Sons, Ltd.

DOI: 10.1002/cnm

Table III. Start instants (t_n) for cycles $n = 1 \ldots 16$ computed in [2]. For the collision cycles 10–16, the interval is also indicated in which the deformed location of $\vec{X}_\text{C}$ has compressive normal traction.

Cycle n [-]	t_n [s]	Cycle n [-]	t_n [s]	$[t_{c,n}, t_{o,n}]$ [s]
1	0.19030	9	0.23792	
2	0.19624	10	0.24386	[0.24682, 0.24682]
3	0.20212	11	0.24994	-
4	0.20812	12	0.25590	-
5	0.21410	13	0.26188	[0.26456, 0.26504]
6	0.22014	14	0.26782	[0.27048, 0.27110]
7	0.22608	15	0.27390	[0.27642, 0.27704]
8	0.23198	16	0.27986	[0.28224, 0.28298]

Copyright © 2013 John Wiley & Sons, Ltd.

Table IV. Reference points on the mid-coronal plane ($X_{\mathrm{ap}} = 0$) of the left VF.

Reference Point	X_{is} [mm]	X_{ml} [mm]
$\vec{X}_{\mathrm{SS}}$	0.00	-1.86
$\vec{X}_{\mathrm{C}}$	-0.740	-0.294
$\vec{X}_{\mathrm{I}}$	-2.71	-4.48
$\vec{X}_{\mathrm{Up}}$	0.00	-5.82
$\vec{X}_{\mathrm{Dn}}$	-5.58	-2.94

Copyright © 2013 John Wiley & Sons, Ltd.

Prepared using cnmauth.cls

Table V. Numerical values of approximation coefficients.

Coefficient	Value	Units
a_1	6.91×10^{-3}	[$\mathrm{s^{-1}Pa^{-1}}$]
a_2	-1.66×10^{-6}	[$\mathrm{ms^{-1}Pa^{-1}}$]
b_1	36.7	[$\mathrm{s^{-1}}$]
c_1	-14.2	[$\mathrm{m^{\frac{1}{2}}s^{-1}}$]
c_2	-9.11×10^{-3}	[$\mathrm{m^{\frac{3}{2}}s^{-1}}$]

Copyright © 2013 John Wiley & Sons, Ltd.

DOI: 10.1002/cnm

Table VI. Scaling parameters used to analyze three cases of interstitial flow development.

Case	$\bar{p}$ [Pa]	$\Delta u_{\mathrm{ml},0}(\vec{X}_{\mathrm{SS}})$ [mm]	$u_{\mathrm{ml},C0}(\vec{X}_{\mathrm{SS}})$ [mm]
1	1000	-0.245	0.00
2	1000	-0.490	0.00
3	1000	-0.735	0.245

Copyright © 2013 John Wiley & Sons, Ltd.

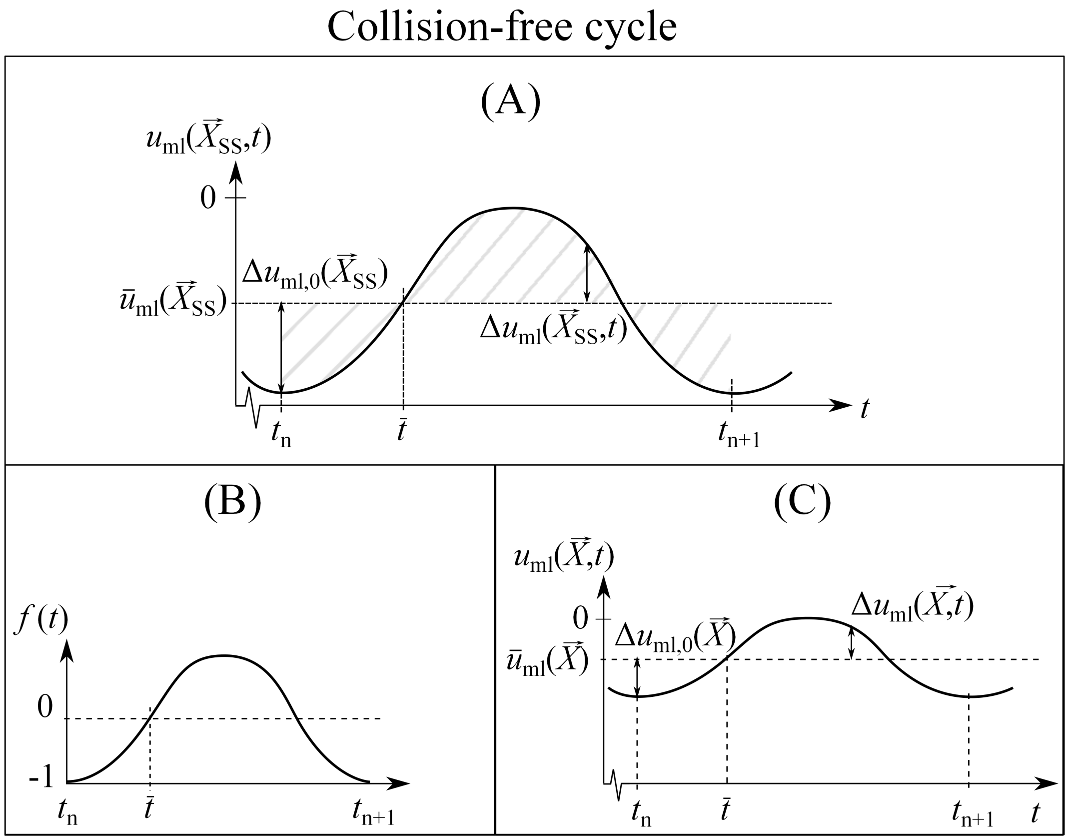

Figure 1. Decomposition of displacements during a vibration cycle without collision. (A) Cycle start and end times (t_n and t_{n+1} respectively) are determined from $u_{\mathrm{ml}}(\vec{X}_{\mathrm{SS}},t)$; the average displacement $\bar{u}_{\mathrm{ml}}(\vec{X}_{\mathrm{SS}})$ is determined such that the area under the curve is zero (shaded); instant $\bar{t}$ corresponds to the first occurence of $\bar{u}_{\mathrm{ml}}(\vec{X}_{\mathrm{SS}})$. (B) The normalized fluctuation about the mean $f(t)$ is used to decompose the hydrostatic stress everywhere. (C) Time instants t_n, t_{n+1} and $\bar{t}$ are used to decompose the displacement at other vocal fold locations.

Copyright © 2013 John Wiley & Sons, Ltd.

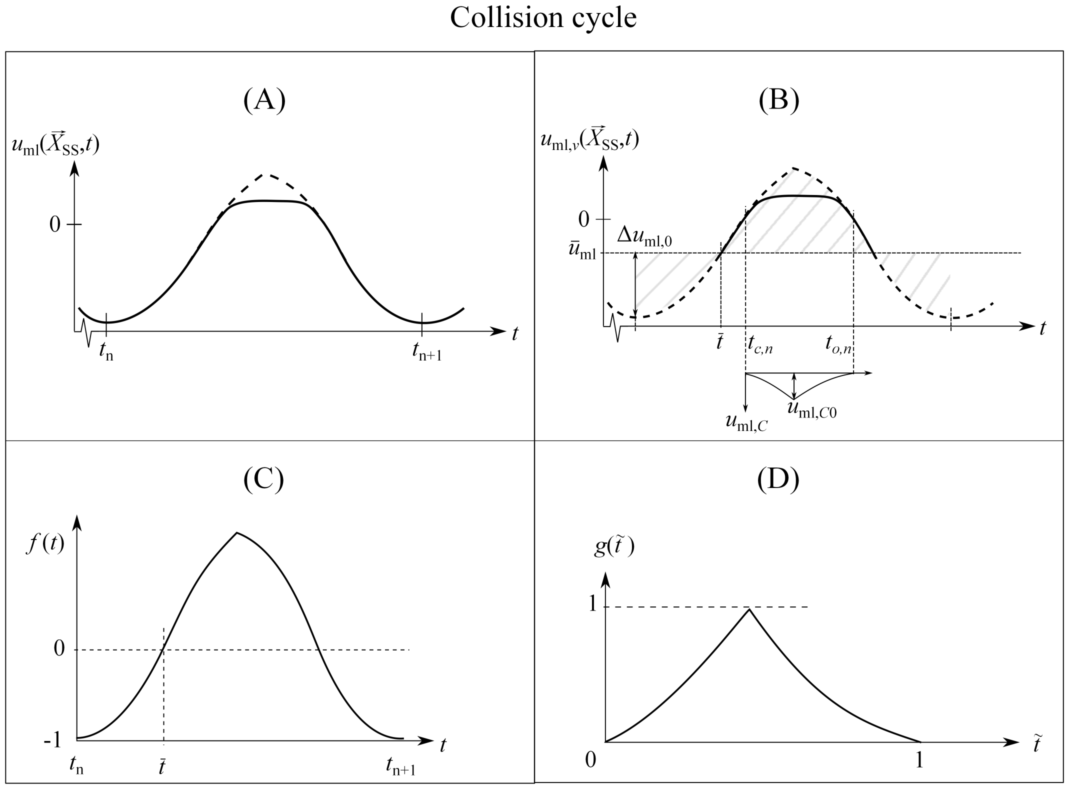

Figure 2. Decomposition of displacements during a vibration cycle with collision. (A) Similar to figure 1 instants t_n and t_{n+1} are determined from $u_{\mathrm{ml}}(\vec{X}_{\mathrm{SS}},t)$ (solid curve); the overclosed cycle $u_{\mathrm{ml},v}(\vec{X}_{\mathrm{SS}},t)$ is estimated (dashed curve). (B) The average displacement $\bar{u}_{\mathrm{ml}}(\vec{X}_{\mathrm{SS}})$, the instant $\bar{t}$ and the function $f(t)$ are based on $u_{\mathrm{ml},v}(\vec{X}_{\mathrm{SS}},t)$; the area between $\bar{u}_{\mathrm{ml}}(\vec{X}_{\mathrm{SS}})$ and $u_{\mathrm{ml},v}(\vec{X}_{\mathrm{SS}},t)$ is zero (shaded); difference between $u_{\mathrm{ml}}(\vec{X}_{\mathrm{SS}},t)$ (dashed curve) and $u_{\mathrm{ml},v}(\vec{X}_{\mathrm{SS}},t)$ equals the collision-induced contribution $u_{\mathrm{ml},C}(\vec{X}_{\mathrm{SS}},t)$ which is zero outside the collision interval $[t_{c,n},t_{o,n}]$. Decomposition of displacement and hydrostatic stressesat other vocal fold locations (not shown) is based on instants t_n, t_{n+1} and $\bar{t}$ along with (C) the normalized function $f(t)$ and (D) the normalized collision-induced contribution $g(\tilde{t})$.

Copyright © 2013 John Wiley & Sons, Ltd.

DOI: 10.1002/cnm

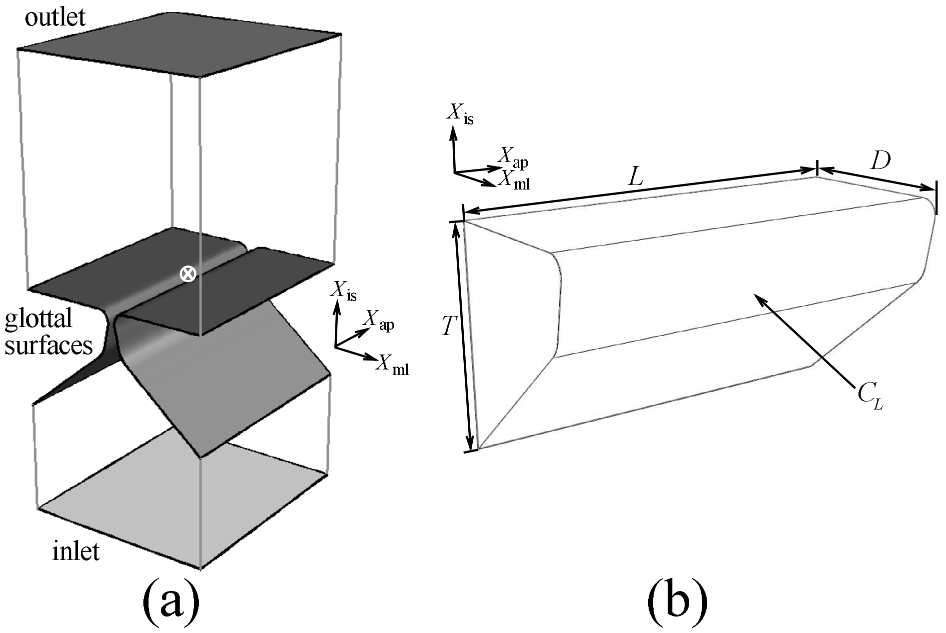

Figure 3. (a) Geometry of the glottal airflow domain. The inlet, outlet and glottal surfaces are shaded. The coordinate origin is denoted by $\otimes$. (b) Geometry of the left half of the VF model. The region C_L is part of the glottal surface that is expected to participate in collision. Coordinate axes are offset from the origin for clarity.

Copyright © 2013 John Wiley & Sons, Ltd.

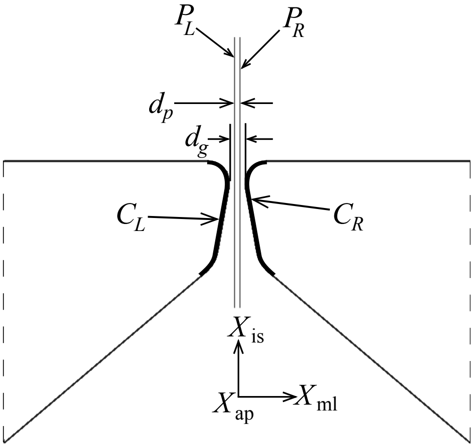

Figure 4. Mid-coronal cross-section showing initial configuration: rigid planes P_L and P_R separated by distance d_p; the left and right VFs separated initially by at least the gap d_g and located symmetrically on either side of the respective rigid planes; and contact surfaces C_L and C_R on respective VFs. Coordinate axes are shown offset from the origin for clarity.

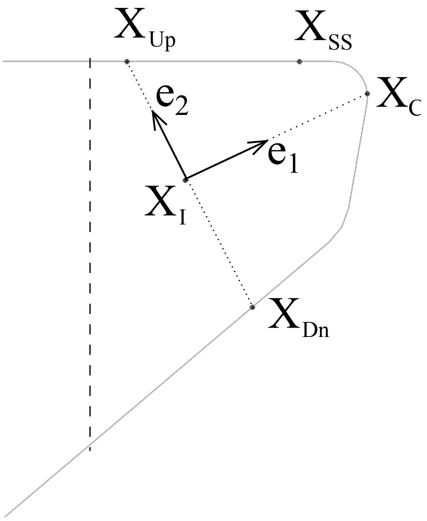

Figure 5. Location of reference points and reference unit vectors on the mid-coronal plane. Dashed line indicates the lateral boundary of the area over which $\nabla \Delta\sigma_{H,0}$ was averaged.

Copyright © 2013 John Wiley & Sons, Ltd.

Prepared using cnmauth.cls

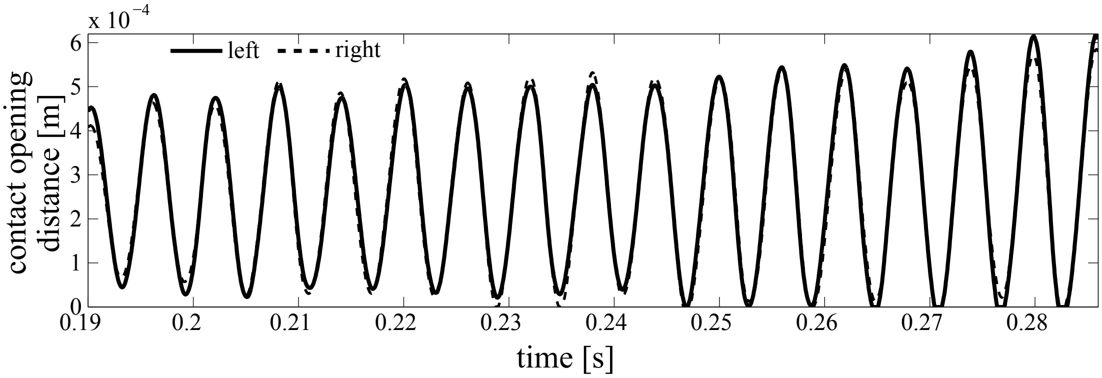

Figure 6. Contact opening distance at mid-coronal plane in dependence of time: solid line, on left vocal fold (VF) defined as $[(d_g - d_p)/2 - u_{\mathrm{ml}}]$ at $\vec{X}_{\mathrm{C}}$; dashed line, on the right VF defined as $[(d_g - d_p)/2 + u_{\mathrm{ml}}]$ at a location similar to $\vec{X}_{\mathrm{C}}$.

Copyright © 2013 John Wiley & Sons, Ltd.

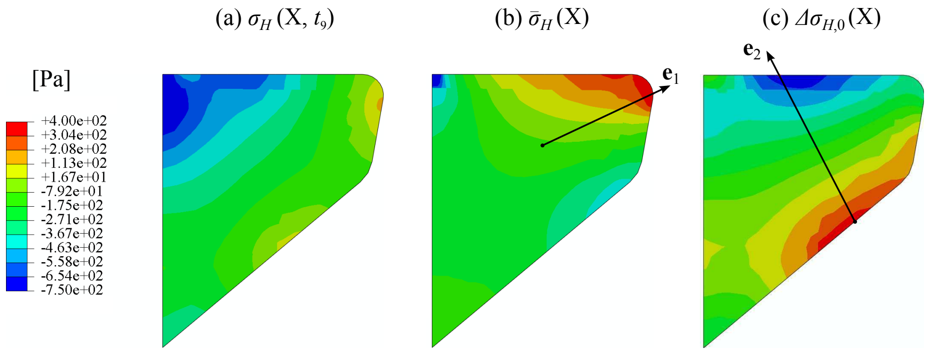

Figure 7. For the vibration cycle 9, contours of (a) instantaneous hydrostatic stress σ_H at maximum open instant t_9, (b) mean hydrostatic stress $\bar{\sigma}_H$, and (c) fluctuation hydrostatic stress $\Delta\sigma_{H,0}$ on the mid-coronal plane. Solid lines in figures (b) and (c) are parallel to unit vectors $\vec{e}_1$ and $\vec{e}_2$ respectively.

Copyright © 2013 John Wiley & Sons, Ltd.
Prepared using cnmauth.cls

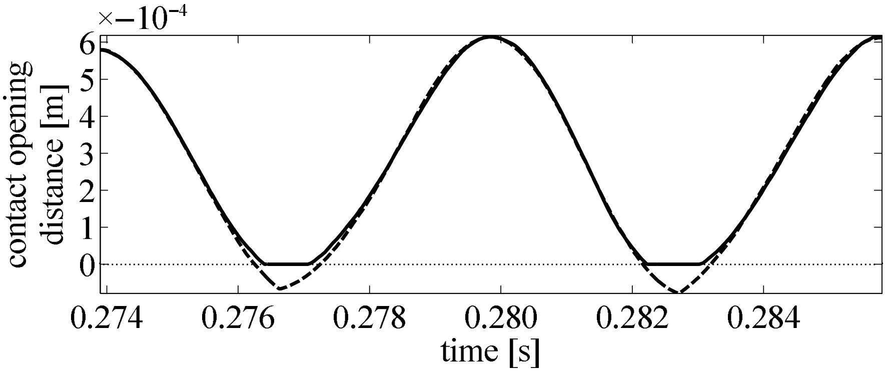

Figure 8. Time development of contact opening distance for collision cycles 15 and 16, where negative values indicate overclosure. Solid line, computed quantity $(d_g - d_p)/2 - u_{\rm ml}(\vec{X}_{\rm C}, t)$; dashed line, virtual quantity $(d_g - d_p)/2 - u_{{\rm ml},v}(\vec{X}_{\rm C}, t)$.

Copyright © 2013 John Wiley & Sons, Ltd.
Prepared using cnmauth.cls

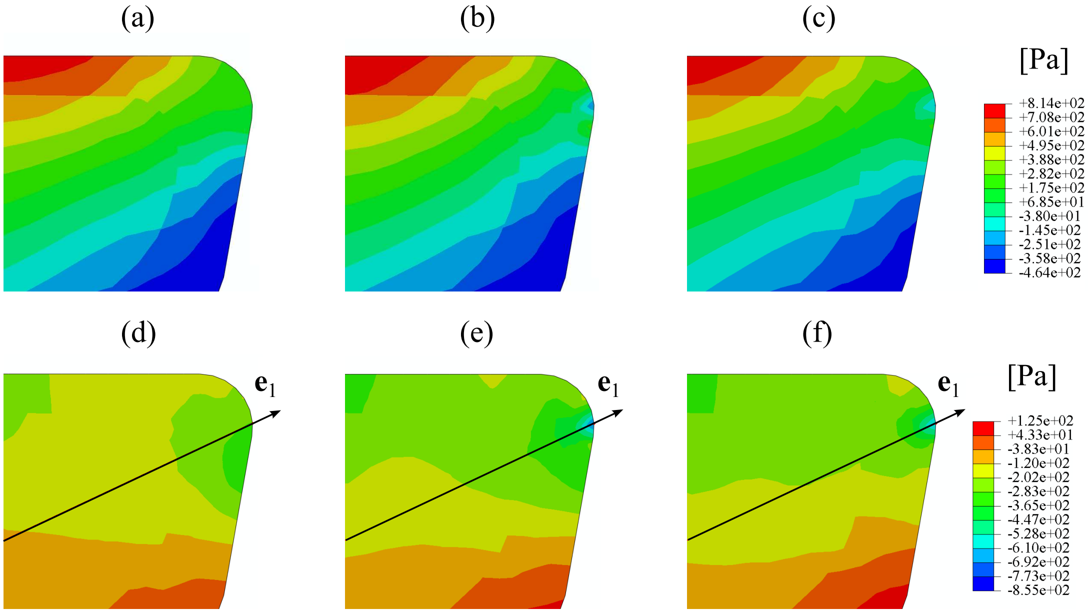

Figure 9. Contours of (a–c) σ_H and (d–f) $\sigma_{H,C}$ at three representative time instants of collision cycle 15. Time instants correspond: (a,d) $t = 0.27640$ s; (b,e) $t = 0.27662$ s; (c,f) $t = 0.27680$ s.

Copyright © 2013 John Wiley & Sons, Ltd.

DOI: 10.1002/cnm

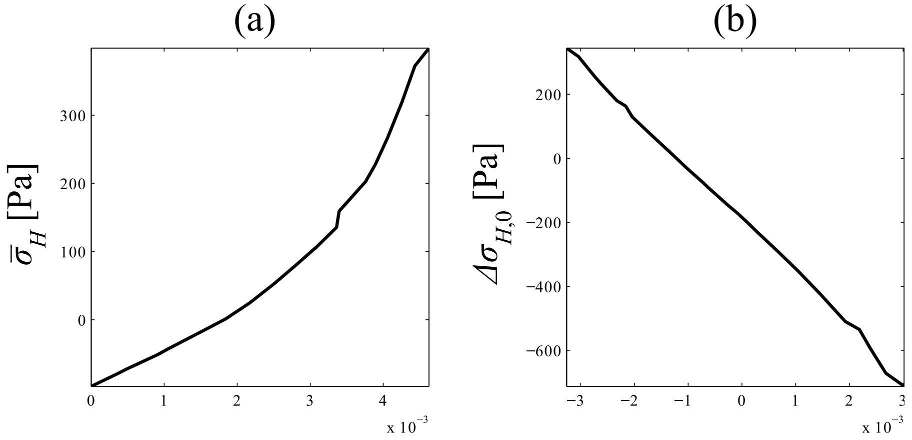

Figure 10. For the vibration cycle 9, variation of (a) $\bar{\sigma}_H$ and (b) $\Delta\sigma_{H,0}$ in dependence of ξ_1 and ξ_2 respectively.

Copyright © 2013 John Wiley & Sons, Ltd.

DOI: 10.1002/cnm

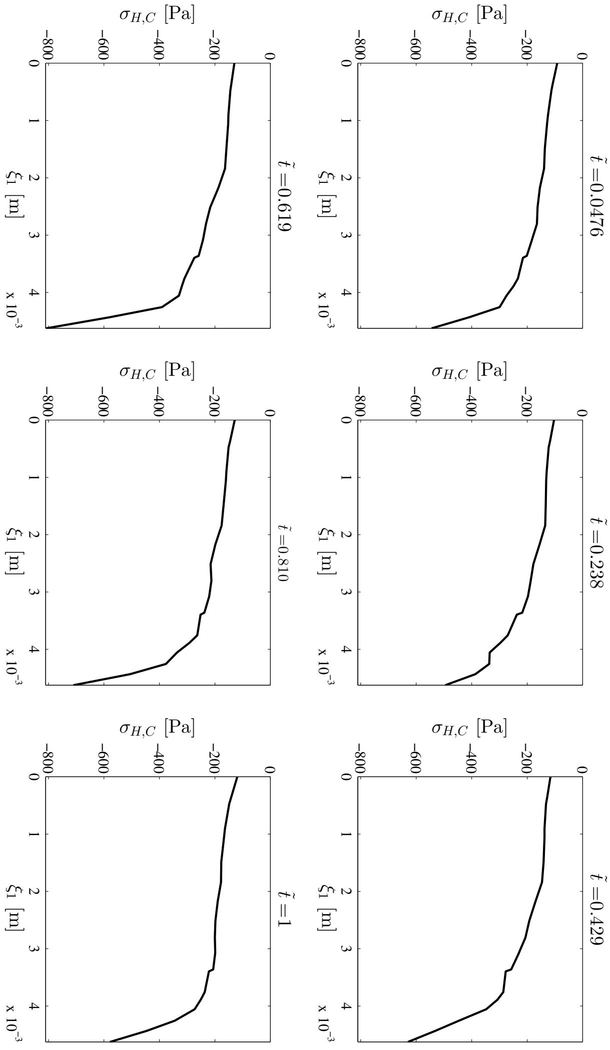

Figure 11. Spatial variation along ξ_1 of contact contribution of hydrostatic stress at 6 equally spaced time instants during active contact in cycle 15.

Copyright © 2013 John Wiley & Sons, Ltd.

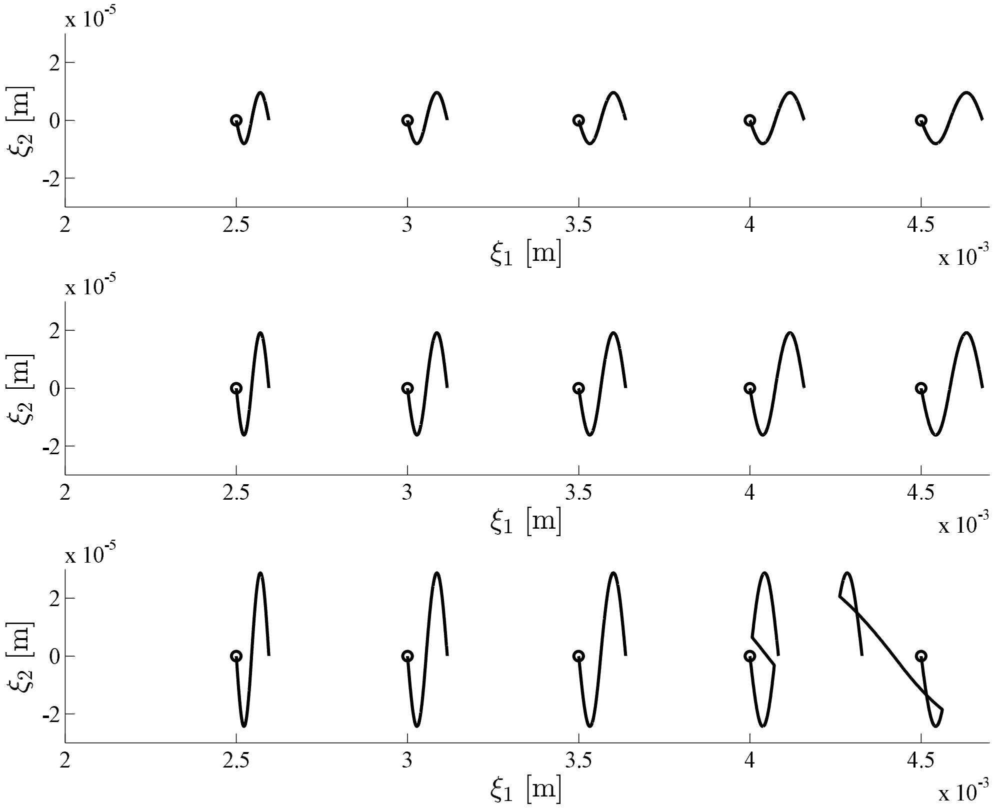

Figure 12. Interstitial fluid particle trajectories on the mid-coronal plane for representative cases: (a) no contact, (b) marginal contact, and (c) significant contact. Circles indicate the initial positions of the fluid particles.

Copyright © 2013 John Wiley & Sons, Ltd.

DOI: 10.1002/cnm

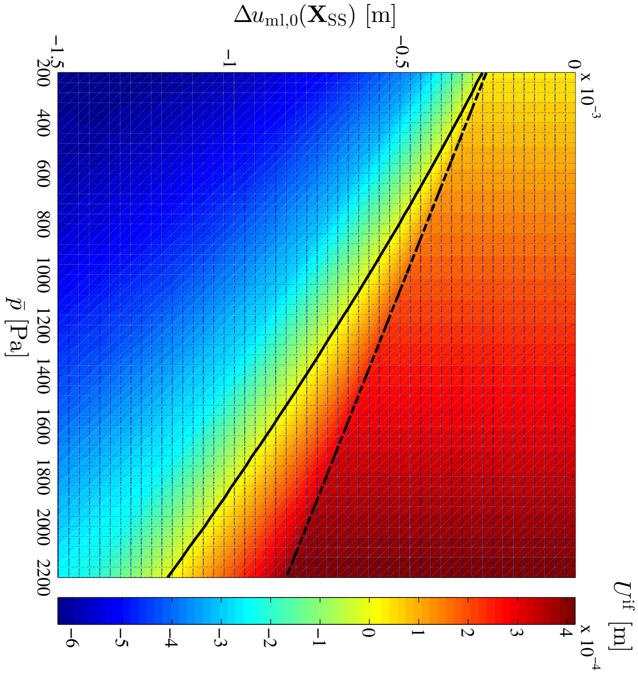

Figure 13. Contours of U^{if} in dependence of $\bar{p}$ and $\Delta u_{\mathrm{ml},0}(\vec{X}_{\mathrm{SS}})$. Here U^{if} is the per-cycle interstitial fluid displacement in the $\vec{e}_1$-direction of a fluid particle located initially at the medial-surface location $\vec{X}_{\mathrm{C}}$, $\bar{p}$ is the average TPD and $\Delta u_{\mathrm{ml},0}(\vec{X}_{\mathrm{SS}})$ is the fluctuation amplitude of medial–lateral displacement at the superior-surface location $\vec{X}_{\mathrm{SS}}$. The dashed and solid lines indicate respectively phonation conditions for which marginal collision and marginal interstitial fluid particle displacement occur.

Copyright © 2013 John Wiley & Sons, Ltd.

DOI: 10.1002/cnm

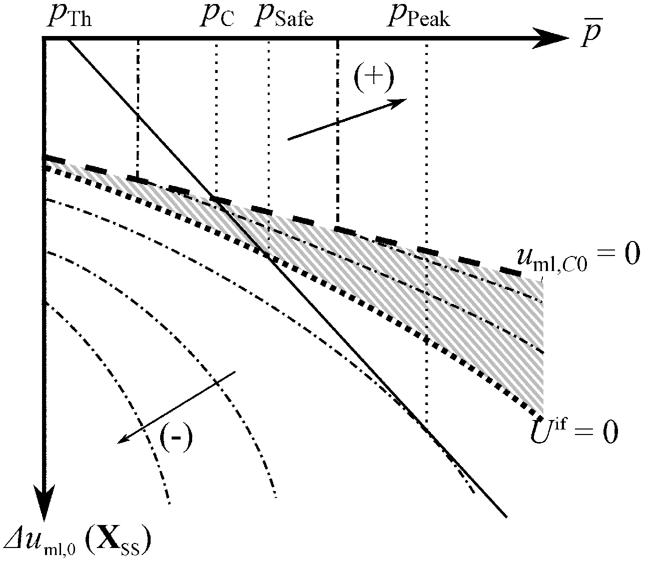

Figure 14. Schematic of hydration map, i.e. contours of U^{if} in dependence of $\bar{p}$ and $\Delta u_{\mathrm{ml},0}(\vec{X}_{\mathrm{SS}})$. Here U^{if} is the per-cycle interstitial fluid displacement in $\vec{e}_1$-direction of a fluid particle located initially at the medial-surface location $\vec{X}_{\mathrm{C}}$, $\bar{p}$ is the TPD and $\Delta u_{\mathrm{ml},0}(\vec{X}_{\mathrm{SS}})$ is the fluctuation amplitude of medial–lateral displacement at the superior-surface location $\vec{X}_{\mathrm{SS}}$. Dash-dotted lines indicate level curves of U^{if}; thick dashed line indicates marginal collision; thick dotted curve indicates zero interstitial fluid displacement; solid straight line indicates physically realizable locus of TPD and fluctuation amplitude (or Titze's line).

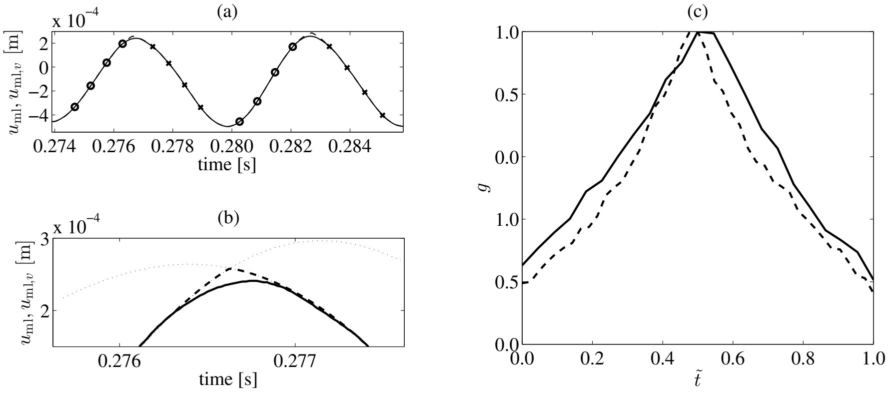

Figure 15. (a) Comparison of u_{ml} (solid line) and $u_{\mathrm{ml},v}$ (dashed line) at $\vec{X}_{\mathrm{SS}}$ in cycles 15 and 16. Circles and crosses respectively denote instants in the closing and opening phases where f is sampled. (b) In a close-up of cycle 15, approximations of closing and opening phases are shown in dotted lines. (c) Comparison of time-dependence of collision-induced functions $g(\tilde{t})$ from cycle 15 (solid line) and cycle 16 (dashed line).

Copyright © 2013 John Wiley & Sons, Ltd.

DOI: 10.1002/cnm